ORBITAL EVOLUTION OF LEVITATED REGOLITH PARTICLES IN THE 65803 DIDYMOS BINARY SYSTEM

Aleksander Fiuk[1], Stefania Soldini[2], Adriano Campo Bagatin[3], Nair Trógolo[4], Jeannette Heiligers[5], [1]Delft University of Technology, Kluyverweg 1, 2629 HS, Delft, The Netherlands, aleksander.fiuk@gmail.com; aleksander.fiuk@gmail.com; [2]University of Liverpool, Brownlow Hill, Liverpool L69 3GH, United Kingdom; [3]UIFACyT, Universidad de Alicante, Carrer Alicante 92, 03690 San Vicente del Raspeig, Alicante, Spain; [4]Observatorio Astronómico, Universidad Nacional de Córdoba, Francisco N. de Laprida 854, X5150 Córdoba, Argentina; [5]Delft University of Technology, Kluyverweg 1, 2629 HS Delft, The Netherlands

Keywords: *Hera, Didymos, regolith particles, levitation, binary asteroid*

Abstract: Operating a spacecraft in a strongly perturbed environment of a binary asteroid system is a challenging task. In this context, risk of collision with free-floating regolith grains is one of the least-studied problems. In light of the near-future exploration of the 65803 Didymos binary system by the Hera probe and the lack of study of orbital evolution of naturally levitated regolith particles in the Didymos system, a method is here proposed to identify such regions of high collision risk. The assessment method comprises (1) determination of regions of regolith levitation from the asteroidal surface, (2) identification of regions of stable motion, i.e., orbital neighborhoods in which particles may survive for extended periods of time, and (3) exploration of the trajectories connecting the initial states upon levitation and the final states in the stable-motion trajectories. Periodic orbits and regions of stable motion are computed through a grid-search method applied in the augmented bicircular problem, i.e., a dynamical model that constitutes an expansion of the bicircular four-body problem by substituting the point-mass gravity fields with spherical-harmonics models of ellipsoidal primaries, applying solar-radiation pressure and third-body perturbances. The investigation of the regions of regolith levitation is conducted using a proximity dynamical model—a modification of the augmented bicircular problem in which the spherical-harmonics gravity field of Didymos is substituted by a mass-concentration model to ensure convergence at the surface of the primary body. The distance between trajectories leading from the off-surface levitation of the grains from the primary body and the trajectories of bounded motion is then assessed. The methodology presented in this work does not render conclusive results with regards to the existence or absence of temporary-capture trajectories in the adopted model. A qualitative evaluation of the expected patterns of motion of regolith particles is here presented together with a discussion of the key conclusions in the context of insitu operations planning for the Hera probe. The primary region of hazard to the spacecraft is identified to be the vicinity of the ecliptic plane of the system. As a result of the study, the Hera spacecraft is found to be under hazard of collision with regolith particles (1) in trajectories escaping from the binary system and (2) in longterm chaotic motion after levitation from Didymos. Existence of two dust disks is suggested, where the inner disk spans up to 20 km from the center of the binary system and the outer disk is formed by the particles slowly spiraling out of the binary system. The inner disk is identified as the larger risk to the spacecraft than the outer one due to its chaotic character and significantly larger expected density.

Nomenclature:

a, b, c	ellipsoid semi-axes [m]
A	orbital semi-major axis [m]
$\underline{A}, \underline{B}, \underline{C}$	factors of a polynomial expression [-]
$C_{k,l}$	Stokes coefficient of k-th degree and l-th order [-]
c_l	speed of light [$\mathrm{m\,s^{-1}}$]
C_p	pressure coefficient [-]
$C_{\mathbf{X}/\mathbf{x}}$	state history matrix of augmented state vector $\mathbf{X}$/state vector $\mathbf{x}$
$\tilde{C}_{\mathbf{X}}$	interpolated state history matrix of augmented state vector $\mathbf{X}$
d	distance [-]
D	semiaxis extent [m]
D^*	semiaxis extent of a Dynamically Equivalent Equal Volume Ellipsoid [m]
$\mathbf{D}$	augmented state space [-]
e	orbital eccentricity [-]
f	mean orbital motion [$\mathrm{rad\,h^{-1}}$]
F, F_S	Cartesian and spherical functions describing an ellisoid [-]
$\mathcal{F}$	reference frame [-]
G	universal gravitational constant [$\mathrm{m^3\,s^{-1}\,kg^{-2}}$]
i	orbital inclination [deg]
m	mass [kg]
M^*	characteristic mass [kg]
n	fraction of a total number of particles N [-]
$\hat{\mathbf{n}}$	normal vector [-]
N	number of particles [-]
R	distance to the Sun [m]

R^*	characteristic distance [m]
r	normalized distance or radius [-]
$\ddot{r}^*$	characteristic acceleration [$\mathrm{m\,s^{-2}}$]
(r, λ, δ)	normalized spherical coordinates: radius, inclination, azimuth [(-,$\deg$,$\deg$)]
$\mathbf{r}$	position vector [-]
$\mathbb{R}$	rotation matrix [-]
s	sigmoid contrast factor [-]
$\hat{\mathbf{S}}$	third body-pointing unit vector [-]
t	time [-]
t^*	characteristic time [s]
T	period [-]
$\mathbf{T}$	translation vector [-]
U	normalized gravity potential [-]
v	speed/magnitude of velocity [-]
V^*	characteristic velocity [$\mathrm{m\,s^{-1}}$]
W_E	solar constant [$\mathrm{W\,m^{-2}}$]
(x, y, z)	Cartesian coordinates [-]
$\mathbf{x}, \mathbf{X}$	state vector and augmented state vector in $\mathcal{F}$
α	experienced slope [$\deg$]
α_e	angle of rotation of an ellipse [$\deg$]
β	SRP effective coefficient [-]
ϵ	relative error [-]
(λ, δ)	longitude, latitude [($\deg$,$\deg$)]
(Λ_b, B_b)	orbital pole coordinates [($\deg$,$\deg$)]
Λ	orientation of the primary body [rad]
μ	mass parameter [-]
$\mu_{D/d}$	normalized mass of Didymos/Dimorphos [-]
$\tilde{\mu}_{D/d}$	finite-density distribution of normalized mass of Didymos/Dimorphos [-]
ϕ	third-body azimuthal position in the synodic frame [rad]
φ	arbitrary real number [-]
ψ	orbital obliquity [$\deg$]
ρ	density [$\mathrm{kg\,m^{-1}}$]
σ	area-to-mass ratio [$\mathrm{m\,kg^{-2}}$]
$\tilde{\sigma}$	sigmoid function [-]
τ	normalized time [-]
$\mathbf{\Omega}$	angular velocity vector of the synodic frame [$\mathrm{rad}/-$]
Ω	angular rate of the synodic frame [$\mathrm{rad}/-$]
Ω_s	revolution rate of a third body [$\mathrm{rad}/-$]

Subscripts

b	related to the binary system
D	Didymos
d	Dimorphos
E	Earth
e	eclipse
ell	ellipsoid
ext	extremum
h	related to the heliocentric orbit
i	generic notation for quantities referring to one of the primaries
l	levitation trajectory-related quantity
min, max	minimum, maximum value
M_D, M_d	related to the non-spherical mass distribution of Didymos/Dimorphos
o	periodic orbit-related quantity
p	related to the test particle
$proj$	projected value
ref	reference value

Superscripts

$*$	characteristic quantity

Other notation

$\dot{\square}$, $\ddot{\square}$	first and second time derivatives, respectively
$\tilde{\square}$	quantity interpolated as a t-function
$\underline{\square}$	dimensional value of a normalized variable $\square$

Introduction: Over recent decades, the scientific community has become ever-more aware of dangers lurking in the depths of outer space. Due to the popularization of the concept of deadly space-born encounters, such as the close-approach event of asteroid Apophis in 2029 [1], the attention of governmental bodies is drawn to Near Earth Asteroids (NEAs), i.e., asteroids with an orbital perihelion within 1.3 AU from the barycenter of the Solar System [2], as their potential encounter with our planet poses a risk to the global population and economy. One of the NEAs subclasses, Potentially Hazardous Asteroids (PHAs), are defined as NEAs (1) of approximately or larger than 150 m in diameter and (2) characterized by a Minimum Orbit Intersection Distance (MOID), i.e., the minimum distance between the trajectories of Earth and the NEA, of less than or equal to 0.05 AU [3]. To prevent the undesirable event of a NEA impact, risk mitigation techniques are investigated and may be divided into deflection and disruption of PHAs. Deflection might be executed by means of (1) abrupt modifications to the NEA's trajectory, e.g., by means of a kinetic impactor or nuclear explosive deflection or (2) slow operation using a gravity tractor, laser ablation of asteroidal material, a rocket engine attached to the asteroid surface, or focused solar energy to exert radiation pressure [3, 4].

To date, only one impact mitigation technique has been demonstrated in a large-scale experiment of the Asteroid Impact and Deflection Assessment (AIDA) - a mission composed of the Double Asteroid Redirection Test (DART) impactor and the European Space Agency's Hera reconnaissance probe. AIDA's goal is to test the kinetic impactor technique as a deflection scenario on the smaller body of the binary asteroid (65803) Didymos, i.e., Dimorphos, and provide insight into the internal structure of the asteroids by studying the post-impact properties of the system [5, 6, 7]. Since both the binary system and its more massive body are named 'Didymos', we refer to them as 'the Didymos system' (or 'the Didymos binary system') and 'Didymos', respectively. The Didymos system was selected for this technology demonstration mission due to its binary nature - the mass of the lesser body of the system is sufficiently small to allow observation of the change in momentum from the impact [5]. DART has performed the impact into the smaller body of the Didymos binary system on September 26th, 2022 [8], during the binary asteroid's close approach to Earth. Hera will arrive at the system in January 2027 [9].

Planning of Hera's trajectory within the binary system requires knowledge of potential hazards and a structured approach to the mitigation thereof. Limited information available on the system introduces large uncertainties in the anticipated state of the system upon the arrival of the spacecraft. One of the potential hazards to the probe may be posed by regolith grains floating in the binary system. To comprehend the risk that the levitated dust poses to the spacecraft, the following phenomena must be considered: (1) trajectories of potential mass transfer between the bodies, (2) temporary capture of levitated regolith grains in periodic orbits or other types of bounded stable motion.

Assuming the presence of loose regolith on the surface of the primaries in the Didymos system - like for other similar small bodies in the Solar System - Cheng et al. [10], Zhang et al. [11], Yu et al. [12], Yu et al. [13] and Yu et al. [14] study the expansion of particles levitated from spinning-top asteroids. Cheng et al. [10] model the observations of ejecta plume as a result of DART's impact, whereas Zhang et al. [11] model interactions between the particles composing internal layers of Didymos. Works by Yu et al. [12, 13, 14] are of particular interest; the authors investigate the Roche lobe properties in the Didymos binary and determine the regions where levitation of non-microscopic particles (particularly of interest in the context of trajectory planning) might occur. The dynamical models used in the studies employ high-accuracy spherical-harmonic expansions of the gravitational field fitted to the radar-derived shapes of the asteroids under the assumption of uniform density distribution, inertial (Coriolis and centrifugal) accelerations, and contact forces. In [13], Yu et al. investigate the re-accretion by Dimorphos of the regolith particles originating from DART's impact into Dimorphos, i.e., the mechanism of the forced primary-to-secondary mass transfer. Yu et al. [14] derive shedding-off conditions for loose debris from the surface of Didymos and elaborate on the dynamical analysis indicating a strong size-sorting effect present in the system. The dynamical model introduced in the work accounts for the gravitational fields of both primaries, solar radiation pressure (SRP), tidal effects due to the gravity of the Sun, and contact forces present in the regolith layer. In [14], the authors trace back the dust particles in orbital motion and conclude that most of them originate from the equatorial bulge of Didymos. Similar conclusions are reached by Sánchez et al. [15] in the study of the top-spin asteroid model introduced by Scheeres [16]. Sánchez et al. [15] derived a scaling law determining the conditions necessary for an asteroid to retain regolith particles on its surface.

Temporary capture of levitated regolith particles in the Didymos system has not been studied to date. However, the existence of periodic orbits or regions of bounded motion (which we collectively refer to as 'bounded trajectories') has been investigated. Dynamical frameworks used in these studies are the circular-restricted three-body problem (CR3BP) and the shape-based three-body problem (SB3BP) with possible augmentations of third-body effects and solar radiation pressure. The SB3BP, also named the 'shape-based circular-restricted three-body problem', augments the CR3BP by substituting the point masses with finite-volume masses of arbitrary shapes [17]. Oliveira and Prado [18] perform a grid search for periodic orbits in the Didymos system within the SRP-augmented CR3BP framework. Capannolo et al. [19] identify several families of Direct Orbits (DO's) and orbits around Equilibrium Points (EP's) using the SB3BP representation of the binary. Jean et al. [20] conduct a search for SRP-compatible orbits in the SRP-augmented SB3BP, whereas Dell'Elce et al. [21] and Lasagni Manghi et al. [22] perform analogous analyses in the SB3BP augmented by introducing third-body effects as well as the SRP perturbation. Silva Neto et al. [23] use a high-fidelity model, incorporating the SRP effect and third-body accelerations of all the planets in the Solar System into the SB3BP framework. In conclusion, the dynamical neighborhood of the binary has been extensively studied; however, no comprehensive search for bounded trajectories and temporary capture of the levitated regolith particles therein have been conducted in a high-fidelity model of the Didymos system to date. We deem it a knowledge gap in light of the significant contributions of perturbative accelerations of SRP, nonspherical mass distribution of both bodies, and third-body effects, as shown by Yu et al. [24].

This work thus focuses on determining the conditions leading to temporary capture of naturally-levitated regolith particles within the system using a high-fidelity model. Since natural levitation of regolith particles is expected from Didymos [12, 14], only the primary body of the binary system is considered as the source of regolith shedding. The first investigated aspect is the regions of levitation, which can also serve as validation of the results by Yu et al. [12, 14], who used a detailed shape model of Didymos, accounted for the inertial effects due to the primary's rotation, and surface friction. As a second input to the analysis, we conduct a search of the state space for bounded trajectories by means of a grid search method. In the grid search exploration, we aim to identify regions of bounded motion, which we further investigate as potential initial conditions of periodic orbits. We conclude by performing an intersection of the two results, i.e., the set of initial conditions on the surface leading to levitation and the set of initial conditions leading to the temporary capture in bounded trajectories. As a result of the latter, we obtain a set of initial conditions originating on the surface of the asteroid that lead to temporary capture of dust particles. Since the characteristics of the superficial regolith in the Didymos system are derived from literature-based data under assumption of similarity to other asteroidal regolith layers, we perform the study for only one particle size, as a matter of demonstration of the adopted methodology. In particular, for comparison with the work by Wiegert [25], we perform the study for a diameter of the regolith boulders of 5 cm, which falls within the spectrum of dust properties on similar bodies, as in [26, 27, 28] but does not cover the lesser sizes. We anticipate that the results of this study will make a contribution to the knowledge of the Didymos system and provide valuable input to the planning of Hera's trajectory in the system by determining unsafe-to-fly regions.

Properties of the Didymos system: From the discovery in 1996 by Joe Montani at the Kitt Peak National Observatory, Didymos was considered a single asteroid until the observation of a lesser body, Dimorphos, in a mutual orbit with the main body in 2003 by Petr Prevc of the Ondřejov Observatory [29, 30]. The Didymos system has been studied by means of photometric lightcurve analysis [31] and planetary radars [32]. The large size of Didymos allowed for precisely describing its physical properties (see tab. 1), including a radar-derived shape model of the asteroid [33]. However, the physical features of Dimorphos determined by the aforementioned analyses bear larger uncertainties (see tab. 2) due to a small signal-to-noise ratio in the radar imaging [34]. Based on previous knowledge of other binary asteroids, Agrusa et al. [33] conclude that the Didymos system secondary body is in a 1:1 spin-orbit ratio, i.e., in tidal lock. Simulations conducted by the authors of [33] indicate that - depending on DART's impact scenario - Dimorphos might break out of its resonance or enter libration.

Tab. 3 lists the physical properties of the Didymos system - from its mass, size ratio, and characteristics of the binary system orbit to its orbital data in the the heliocentric ecliptic J2000 reference frame [29]. Tab. 1 presents a collection of Didymos' physical properties: its bulk density, shape, and rotation period. Note that the Dynamically Equivalent Equal Volume Ellipsoid (DEEVE) in tab. 1 is "an ellipsoid with uniform density with the same volume and moments of inertia as the shape model" [32] and will be used for dynamical modelling. Damme et al. [35] computed the $C_{2,0}$ and $C_{2,2}$ Stokes coefficients of the spherical harmonic expansion of the gravitational field from the radar-derived shape model of Didymos and assuming it to be a tri-axial ellipsoid (see fig. 1) of constant density. The principal axes of Dimorphos' tri-axial ellipsoid $a_d > b_d > c_d$ are defined through mutual ratios (see tab. 2). The semi-axes of Dimorphos' DEEVE were calculated from the assumption that D_d is the diameter of a uniform-density ball, whose mass is equal to the mass of an ellipsoid characterized by the axes ratios a_d/b_d and b_d/c_d. The density of the regolith grain on the surface of Didymos is assumed to be equal to the bulk density of this asteroid, as given in tab. 1.

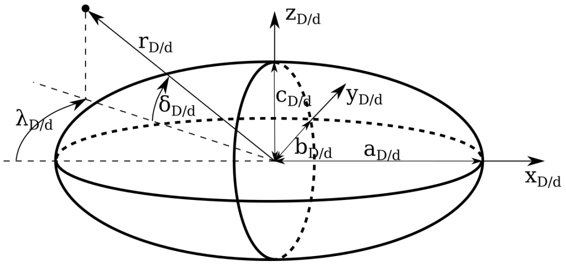

Figure 1: Ellipsoid

Table 1: Properties of Didymos

Physical quantity	Symbol	Value	Unit	Comments and references
Bulk density	ρ_D	2170 ± 350	kg m^{-3}	Based on D_D and m_b [36, 6, 37]
Extents along principal axes	D_{D,x_D} D_{D,y_D} D_{D,z_D}	$832 \pm 6\%$ $838 \pm 6\%$ $786 \pm 10\%$	m	[32]
DEEVE extents	D^*_{D,x_D} D^*_{D,y_D} D^*_{D,z_D}	$797 \pm 6\%$ $783 \pm 6\%$ $761 \pm 10\%$	m	[32]
$C_{2,0}$ coeff. unnormalized	$C_{2,0}$	-0.023	-	Assuming constant density and tri-axial ellipsoid shape [35]
$C_{2,2}$ coeff. unnormalized	$C_{2,2}$	-0.0013	-	Assuming constant density and tri-axial ellipsoid shape [35]
Sidereal spin period	$\underline{T}_D$	2.2600 ± 0.0001	h	[32]

Table 2: Properties of Dimorphos

Physical quantity	Symbol	Value	Unit	Comments and references
Ellipsoidal axes ratios	a_d/b_d b_d/c_d	1.3 ± 0.2 1.2 ± 0.2	-	Based on other binary systems [38, 6, 36]
Equivalent diameter	D_d	$164 \pm 11\%$	m	From D_D and D_d/D_D [36]
DEEVE extents	D^*_{d,x_d} D^*_{d,y_d} D^*_{d,z_d}	213.50 164.22 136.86	m	Calculated assuming equal mass to a sphere of diameter equal to D_d and uniform ellipsoidal density distribution

Dynamical model: Damme et al. [35] presented a quantitative comparison of the magnitudes of various accelerations in the vicinity of the Didymos system. In view of the small mass of the system, the third-body (also referred to as 'tidal') effects due to the Sun's mass and the SRP perturbation have a large contribution to the total acceleration experienced by the particle. Therefore, the augmented bicircular problem (ABP) is used for the dynamics of levitated particles in this work. The ABP is the combination of the SB3BP and the SRP-augmented bicircular problem (BP). The dynamical model introduces ellipsoidal primaries - a rotating primary and a tidally locked secondary as in Ferrari et al. [17] - as well as gravitational third-body and SRP perturbations, as given by Heiligers and Scheeres [39].

The model is based on the following assumptions: (1) two of the bodies (here, the primaries) have significantly larger mass than the third one (from here on referred to as a 'particle'), (2) gravitation of the particle does not cause observable effects in the motion of the primaries, and (3) the orbits of the primaries are circular. Applying such simplifications in our work is justified by the small individual masses of the regolith particles compared to the scale of the binary and the observed small eccentricity of the binary orbit (see tab. 3). The reference frame is barycentric, i.e., the origin coincides with the center of mass of the primaries. We introduce the mass parameter [40, 41] $\mu = m_d/(m_D + m_d)$, where m_D and m_d are the masses of the primary and secondary, i.e., the more and the less massive bodies, respectively. Normalization of relevant physical quantities is performed using the characteristic dimensions presented in tab. 4 (where G stands for the universal gravitational constant), as in $\zeta = (\zeta^*)^{-1}\underline{\zeta}$, where $\underline{\zeta}$ and ζ^* are a dimensional arbitrary quantity and its characteristic value, respectively. Normalized masses of the primaries are given by [40, 41] $\mu_D = 1 - \mu$ and $\mu_d = \mu$, where $\mu_D \geq \mu_d$. Adopting a synodic reference frame $\mathcal{F}(x, y, z)$ rotating uniformly at a normalized angular rate $\Omega = 1$, where the origin coincides with the center of mass of the binary, the x-axis pierces the centers of mass of both bodies of the binary system, the z-axis is parallel to the system's angular momentum vector, and the y-axis completes the right-hand reference frame, allows

Table 3: Properties of the Didymos system

Physical quantity	Symbol	Value	Unit	Comments and references
Size ratio	D_d/D_D	0.21 ± 0.01	-	[38, 6]
Total system mass	m_b	$(5.28 \pm 0.54) \times 10^{11}$	kg	[6]
Binary orbit				
Semi-major axis	A_b	1.19 ± 0.03	km	[32]
Orbital eccentricity	e_b	< 0.03	-	[38, 6]
Orbital pole	(Λ_b, B_b)	$(310, -84) \pm (0, 9)$	°	[6, 32]
Orbital period	$\underline{T}_b$	$11.920\ {}^{+0.004}_{-0.006}$	h	[6]
Orbital obliquity	ψ_b	171 ± 9	°	[6]
Heliocentric orbit				
Semi-major axis	A_h	1.644576707340323	au	1σ: 5.6956×10^{-9} [29]
Orbital eccentricity	e_h	0.3836383357953901	-	1σ: 9.7517×10^{-9} [29]
Orbital inclination	i_h	3.407819057354463	°	1σ: 3.0891×10^{-6} [29]
Orbital period	$\underline{T}_h$	770.3349979813357	d	1σ: 4.0018×10^{-6} [29]

for fixing the primary at $\mathbf{r}_D = [-\mu, 0, 0]^T$ and the secondary at $\mathbf{r}_d = [1-\mu, 0, 0]^T$ (see fig. 2).

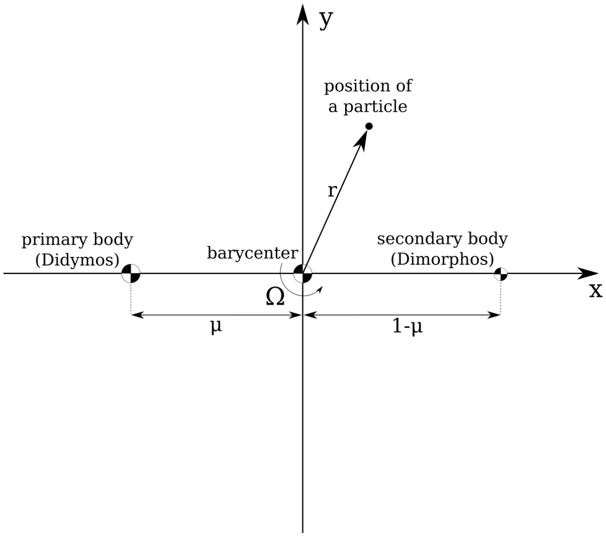

Figure 2: Synodic reference frame

Equations of motion

The equations of motion are defined as

$$\begin{aligned}\ddot{\mathbf{r}} &= -2\,\boldsymbol{\Omega} \times \dot{\mathbf{r}} + \nabla U = \\ &= -2\,\boldsymbol{\Omega} \times \dot{\mathbf{r}} + \nabla U_{SB3BP} + \nabla U_{3rd} + \nabla U_{SRP}\ ,\end{aligned} \tag{1}$$

where

$$\nabla = \left[\frac{\partial}{\partial x}, \frac{\partial}{\partial y}, \frac{\partial}{\partial z}\right]^T \tag{2}$$

and U, U_{SB3BP}, U_{3rd}, and U_{SRP} are the effective potentials of the ABP, of the shape-based three-body problem, of the third-body perturbation, and of the solar-radiation pressure perturbation, respectively; the effective potentials are discussed in detail in the following section.

Effective potential

The effective potential of the augmented bicircular problem (ABP) is composed of three terms: the effective potential of the shape-based three-body problem (SB3BP) U_{SB3BP}, the third-body augmentation term U_{3rd}, and the SRP augmentation term U_{SRP},

$$U = U_{SB3BP} + U_{3rd} + U_{SRP}\ . \tag{3}$$

The effective potential of the SB3BP is given by

$$U_{SB3BP} = \frac{1}{2}\left(x^2 + y^2\right) + U_{M_D} + U_{M_d}\ , \tag{4}$$

where U_{M_D} and U_{M_d} are the gravitational potentials of Didymos' and Dimorphos' ellipsoids, respectively.

Gravitational potential

The Didymos-fixed Cartesian reference frame $\mathcal{F}_D(x_D, y_D, z_D)$ is defined by the origin coincid-

Table 4: Normalization of physical quantities [41]

	Mass [kg]	Distance [m]	Time [s]	Speed [m s^{-1}]	Acceleration [m s^{-2}]
Characteristic value	$M^* = m_b$	$R^* = A_b$	$t^* = 2\pi\left(\frac{(R^*)^3}{(m_b\, G)}\right)^{1/2}$	$V^* = \frac{R^*}{t^*}$	$\ddot{r}^* = \frac{R^*}{(t^*)^2}$

ing with the center of mass of the body, the x_D-axis points along the longest semi-axis of the ellipsoid a_D, the z_D-axis points along the shortest semi-axis c_D of the ellipsoid and in the direction of the z-axis, whereas the y_D-axis completed the right-handed reference frame (see fig. 1). The Dimorphos-fixed reference frame is defined in an analogous manner using the subscripts 'd' - all the body-fixed definitions given below also follow the same analogy between Didymos ('D') and Dimorphos ('d'). All position vector transformations between the synodic and body-fixed reference frames are given in section . The gravitational potentials of the primaries are given in the body-fixed spherical reference frames - for Didymos it reads $\mathcal{F}_{s_D}(r_D, \lambda_D, \delta_D)$, where r_D is the distance to the center of mass of Didymos, λ_D is the azimuth angle, and δ_D is the elevation angle (see fig. 1) given by

$$\lambda_D = \arctan\left(\frac{y_D}{x_D}\right) \tag{5}$$

$$\delta_D = \arcsin\left(\frac{z_D}{r_D}\right)\ , \tag{6}$$

The gravitational potential of Didymos is given by a second-degree, second-order expansion of the spherical harmonics gravity model [42]

$$\begin{aligned} &U_{M_D}(r_D, \delta_D, \lambda_D) = \\ &= \frac{\mu_D}{r_D}\left[1 + \left(\frac{r_{ref,D}}{r_D}\right)^2 \left\{C_{2,0}\left(1 - \frac{3}{2}\cos^2(\delta_D)\right) + \right.\right. \\ &\qquad \left.\left. + 3C_{2,2}\cos^2(\delta_D)\cos(2\lambda_D)\right\}\right]\ , \end{aligned} \tag{7}$$

where $r_{ref,D}$ is the reference radius of Didymos' expansion - in this case $r_{ref,D} = a_D$ due to the coincidence of the expansion origin with the center of mass lying at the center of the ellipsoid.

Perturbative potential of the third-body effect

The relative motion of the Sun in the synodic frame is approximated by a circular orbit at the normalized distance $r_3 = \underline{r}_3\ L^{-1}$ (see fig. 3 and tab. 4) and revolves around the frame's origin at the rate

$$\Omega_s = \frac{f_b + f_h}{f_b} = \left(T_b^{-1} + T_h^{-1}\right) T_b\ , \tag{8}$$

where T_b and T_h are given in tab. 3 f_b and f_h are the mean motion of the binary and heliocentric orbits, respectively. Therefore, the third-body and SRP accelerations act parallel to the Sun-pointing vector $\hat{\mathbf{S}}$, i.e., a unit vector originating at the origin of $\mathcal{F}_s$ and pointing towards the current position of the Sun, which in $\mathcal{F}_s$ takes the form

$$\hat{\mathbf{S}} = \begin{bmatrix}\cos(\phi)\\ \sin(\phi)\\ 0\end{bmatrix} = \begin{bmatrix}\cos(\Omega_s t + \phi_0)\\ \sin(\Omega_s t + \phi_0)\\ 0\end{bmatrix} \tag{9}$$

where $\phi_0 = \phi(t = 0)$, i.e., the angular position of the Sun ϕ in $\mathcal{F}$ at $t = 0$. As shown by the coordinates of the orbital pole of the binary (Λ_b, B_b) in tab. 3, the angular momentum vector of the Didymos binary is opposite to the angular momentum vector of the heliocentric orbit. Therefore, the Sun revolves around the binary in a counter-clockwise fashion in the synodic frame $\mathcal{F}$.

The third-body perturbation produces the difference in the gravitational accelerations experienced by the center of mass of the Didymos binary and the particle due to the difference in distance to the Sun [41, 39]

$$U_{3rd} = \frac{1}{\|\mathbf{r}_4\|} - \frac{\mathbf{r}\cdot\mathbf{r}_3}{r_3^3}\mu_3\ , \tag{10}$$

where μ_3 is the mass parameter of the perturbing fourth body and the vectors $\mathbf{r}$, $\mathbf{r}_3$, and $\mathbf{r}_4$ are the position vector of the particle in $\mathcal{F}$, the position vector of the Sun in $\mathcal{F}$, and the particle-Sun vector in $\mathcal{F}$, respectively,

$$\mu_3 = \frac{m_3}{m_D + m_d} \tag{11}$$

$$\mathbf{r}_3 = r_3\hat{\mathbf{S}} \tag{12}$$

$$\mathbf{r}_4 = \mathbf{r}_3 - \mathbf{r} \tag{13}$$

where m_3 is the Sun's mass (see fig. 3).

Perturbative potential of the solar radiation pressure

The solar radiation pressure (SRP) perturbation is caused by the exchange of momentum between the particle's surface and photons. Effects caused by radiation pressure of sources other than direct illumination by the Sun are neglected. Due to the

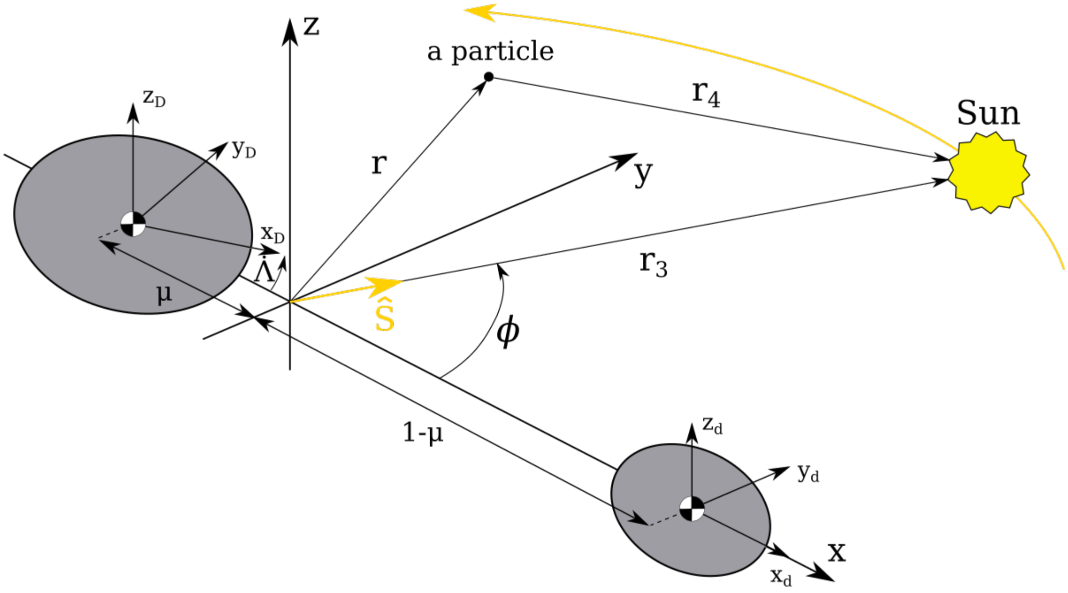

Figure 3: Augmented bicircular problem

use of the shape-based approach, eclipses occur in the model. Therefore, we introduce an eclipse model which serves to calculate the fraction of the SRP acceleration exerted on the particle. The eclipse model follows the cylindrical model as defined by Li et al. [43], where penumbra conditions are not considered (see fig. 4). We define the potential of the SRP perturbation as

$$U_{SRP} = -\ddot{r}_{SRP}(\hat{\mathbf{S}} \cdot \mathbf{r}) \ . \tag{14}$$

The total experienced SRP acceleration is given by

$$\ddot{r}_{SRP} = \ddot{r}_{SRP,BP} \ \beta_D \beta_d \ , \tag{15}$$

where $\ddot{r}_{SRP,BP}$ is the magnitude of unshaded SRP acceleration, β_D and β_d are the effective coefficients due to the shadow cast by the Didymos and Dimorphos, respectively. The shading effective coefficient β is discussed in the following paragraph. The dimensional value of the unshaded SRP perturbation $\underline{\ddot{r}}_{SRP,BP}$ is assumed to be constant over the time scale of the dynamical problem, but varies depending on the exact location of the binary system in its heliocentric orbit, therefore the importance of the eccentricity of the heliocentric orbit ($e_h \approx 0.38$, see tab. 3) cannot be neglected. The normalized magnitude of the SRP acceleration reads [44]

$$\ddot{r}_{SRP} = \left((t^*)^2 (R^*)^{-1} \right) \underline{\ddot{r}}_{SRP,BP} = \\ = \left((t^*)^2 (R^*)^{-1} \right) \frac{W_E C_p \sigma}{c_l} \left(\frac{R_E}{R_b} \right)^2 \tag{16}$$

where $\left((t^*)^2 (R^*)^{-1} \right)$ is the normalizing factor and W_E, C_p, σ, c_l, R_E, R_b are the solar constant, scaling coefficient, mass-to-area ratio of the particle, speed of light, reference Sun-Earth distance, and Sun-Didymos system distance, respectively. The particles are assumed to be of spherical shape and the scaling coefficient is taken as $C_p = 1.5$, whereas for the mass-to-area ratio we use [45]

$$\sigma = \frac{2}{3} \rho \pi r_p \ \ , \tag{17}$$

where ρ is the density of the regolith particle ($\rho = \rho_D$, see 1) and r_p is the particle's radius. Tab.

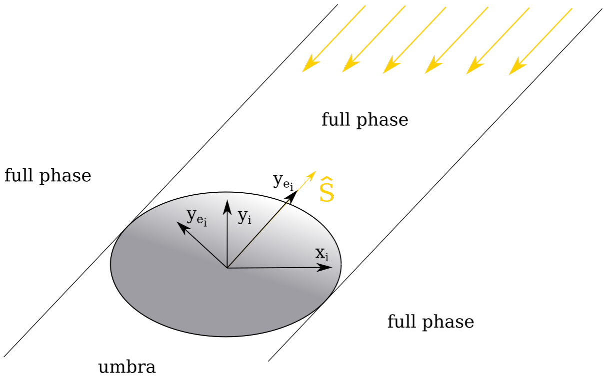

Figure 4: Cylindrical eclipse model

The effective coefficient for Didymos is found from

$$\beta_D = 1 - \tilde{\sigma}\left(5, \frac{r_{ell}(\lambda_D, \delta_D) - r_{proj}}{r_p}\right) \cdot \\ \cdot \, \mathtt{int}\Big((\mathbf{r} - \mathbf{r}_D) \cdot \hat{\mathbf{S}} < 0\Big) \quad (18)$$

where $r_{ell}(\lambda_D, \delta_D)$, r_{proj}, r_p, and $\mathbf{r}_D$ are the radius of the ellipsoid in the direction specified by a pair of spherical coordinates (λ_D, δ_D), the radius projected on the x_D-y_D plane, the radius of the particle, and the position vector in $\mathcal{F}_D$, respectively (for details refer to section). The term $\mathtt{int}\Big((\mathbf{r} - \mathbf{r}_D) \cdot \hat{\mathbf{S}} < 0\Big)$ is a conditional switch, which ensures that the subtrahend of the equation is null if the particle is placed between the luminous body and the (potentially) obscuring body. The modified sigmoid function $\tilde{\sigma}(s, \varphi)$ is defined as [46, 47]

$$\tilde{\sigma}(s, \varphi) = \frac{1}{1 - e^{-s\varphi}} \quad (19)$$

where s is the sigmoid contrast factor and φ is an arbitrary real number. The role of the contrast factor is to allow tailoring the topology of the sigmoid function to the characteristics of the problem. To obtain $\beta_D \approx 1$ for unobscured particles and $\beta_D \approx 0$ for particles in eclipse, we select $s = 5$, and as a result the topology of the modified sigmoid takes the form presented in fig. 5. The larger and smaller dips visible in fig. 5 around $x = 0$ and $x = 1100$ are shades of Didymos and Dimorphos, respectively (the graphical representation of the verification case is given in fig. 6). The use of a smooth function emulates partial shading of the particles when in the transition between full phase and umbra conditions and avoids abrupt changes offered by the Heaviside function [47], often used in the cylindrical model.

Regions of levitation: We determine the regions of levitation by discretizing the ellipsoidal surface and projecting the acceleration vector experienced by a particle on the unit vector normal to the asteroid's surface. This enables us to calculate the slope experienced by the particle. The use of the spherical harmonic expansion of the gravity field is, however, limited to the outside of the Brillouin sphere (BS) [48] - in this study, the BS radius is equal to the largest semi-axis of the DEEVE for both primaries (given in tab. 1 and tab. 2). Therefore, to perform a valid analysis of the dynamics at the surfaces of the ellipsoids, we use a mass-concentration (abbreviated as 'mascon') gravity model (MC) within the BS, which asserts convergence of the gravity field model and has successfully been used to model asteroidal gravity fields [49]. Next, we assess the discontinuity at the BS due to the transition between the newly introduced dynamical model and the ABP. We conclude the analysis by propagating the motion of levitated particles from the surface of an asteroid to the BS or until redeposition on the surface. Further, we study the fates of the particles that cross the BS upon levitation.

Proximity dynamical model

We define the dynamical model (further referred to as the 'proximity dynamical model' or 'PDM') on the surface of the ellipsoidal model of Didymos using a modified effective potential

$$U_{PDM} = U_{MCD} + U_{3rd} + U_{SRP} \ , \quad (20)$$

where the term U_{MCD} describes the effective potential for the particles in the proximity to Didymos's surface, i.e.,

$$U_{MCD} = \frac{1}{2}\left(x^2 + y^2\right) + \sum_{j=1}^{N_{sph}} \left(\frac{\mu_j}{\|\mathbf{r} - \mathbf{r}_j\|}\right) + \\ + \frac{1}{2}\dot{\Lambda}^2 (x_D^2 + y_D^2) + U_{M_d} \ . \quad (21)$$

The terms of eq. 21 are the centrifugal potential of the synodic frame $\frac{1}{2}\left(x^2 + y^2\right)$, the MC potential for Didymos $\sum_{j=1}^{N_{sph}} (\mu_j / \|\mathbf{r} - \mathbf{r}_j\|)$, the centrifugal potential on the surface of Didymos $\frac{1}{2}\dot{\Lambda}^2(x_D^2 + y_D^2)$, and the SH gravity potential of Dimorphos U_{M_d}. N_{sph} is the number of mass concentrations in the model of Didymos and μ_j is the gravitational parameter of the j-th mass concentration, following the constraint $\mu_D = \sum_{j=1}^{N_{sph}} \mu_j$. We investigate only the levitation from rest; therefore, motion on the surface and, as a consequence, the Coriolis acceleration due to the rotation of the body-fixed frames are neglected.

Mechanism of levitation from rest

Levitation of a particle located at (δ_D, λ_D) on the surface of an asteroid is determined by calculating the angle between the acceleration vector $\ddot{\mathbf{r}}_D = \nabla U_{PDM}$ and the inward normal vector $\hat{\mathbf{n}}$, following the approach presented in [14]. The inward normal vector is defined as

$$\hat{\mathbf{n}}(\delta_D(x_D, y_D, z_D), \lambda_D(x_D, y_D, z_D)) = \\ = -\frac{\nabla F}{\|\nabla F\|} \ , \quad (22)$$

where F is a function describing the ellipsoidal model of Didymos in the Didymos-fixed reference

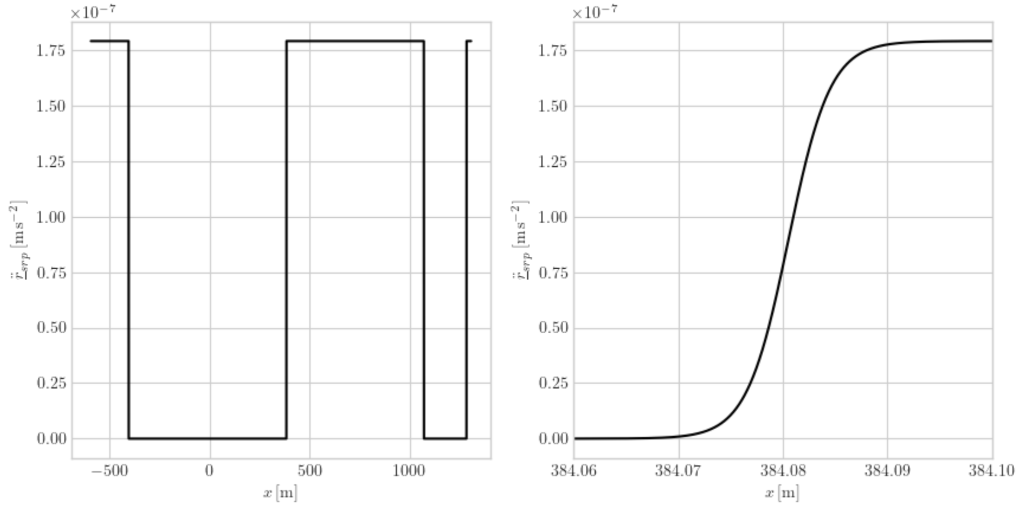

Figure 5: Dimensional values of the SRP acceleration acting on a test particle of radius 1 cm for $\mathbf{r} = [x, -1, 0]^T$, $\phi_0 = \pi/2$, $\Lambda_0 = 0$

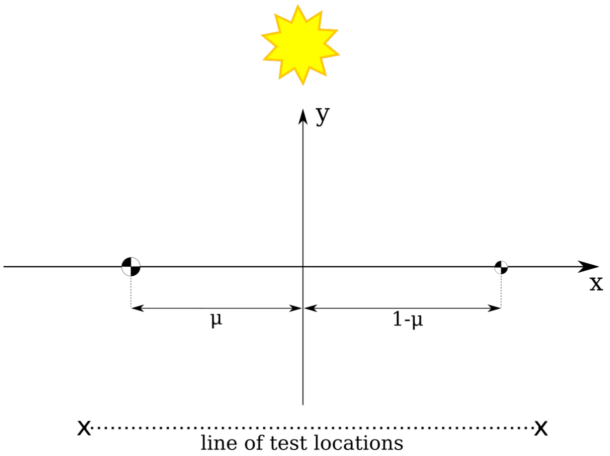

Figure 6: Depiction of the verification case analyzed in fig. 5

frame's Cartesian coordinate system and F_S is an equivalent function using spherical coordinate system in the same reference frame

$$\begin{aligned} F(x_D, y_D, z_D) &= \\ &= F_S\left(\delta_D(x_D, y_D, z_D), \lambda_D(x_D, y_D, z_D)\right) = \\ &= \frac{x_D^2}{a_D^2} + \frac{y_D^2}{b_D^2} + \frac{z_D^2}{c_D^2} - 1 = 0\,, \end{aligned} \tag{23}$$

using a_D, b_D, and c_D, which are the semiaxes of an ellipsoid, whose center of mass coincides with the frame origin and the semiaxes are aligned with the axes of the coordinate frame. The experienced slope of the particle is defined as $\alpha(\delta_D, \lambda_D) = \arccos(\nabla U_{PDM} \cdot \hat{\mathbf{n}}(\delta_D, \lambda_D))$. If $\alpha(\delta_D, \lambda_D) > 90°$, the particle at (δ_D, λ_D) experiences levitation.

Computational model

Didymos is represented by $N_D \approx 12.2 \times 10^6$ uniformly distributed mass concentrations of equal dimensionless elementary gravitational parameters $\mu_j = 8.1073 \times 10^{-8}$. The study of levitation conditions is conducted for all possible combinations of equally spaced four initial azimuthal positions of the Sun ϕ_0 and four initial angular positions of Didymos Λ_0 in the synodic frame of the ABP, i.e., $\phi_0, \Lambda_0 \in \{0,\, \pi/2,\, \pi,\, 3\pi/2\}$. A specific combination of the initial conditions of the system is named a 'case' (for the glossary of all studied cases, see tab. 5). The discretizations yield relative errors of the PDM acceleration (excluding the centrifugal term arising from the rotation of Didymos) with respect to the ABP acceleration on the BS smaller than 1%. The relative error on the BS is defined as $\epsilon_{BSi} = \|\nabla U - \nabla U_{PDM}\| \, \|\nabla U\|^{-1}$ and an example of the resulting error map is presented in fig. 7; we observe the largest relative error in the polar regions, which are the least distanced from the center of mass, and around the most-distanced areas, i.e., surrounding the points on the ellipsoidal surface of Didymos that are pierced by the largest semiaxes a_D.

As found by Yu et al. [14], dust particles located in the equatorial regions of Didymos likely experience levitation. Therefore, we examine only the primary body using a grid size of $1°$ in either lati-

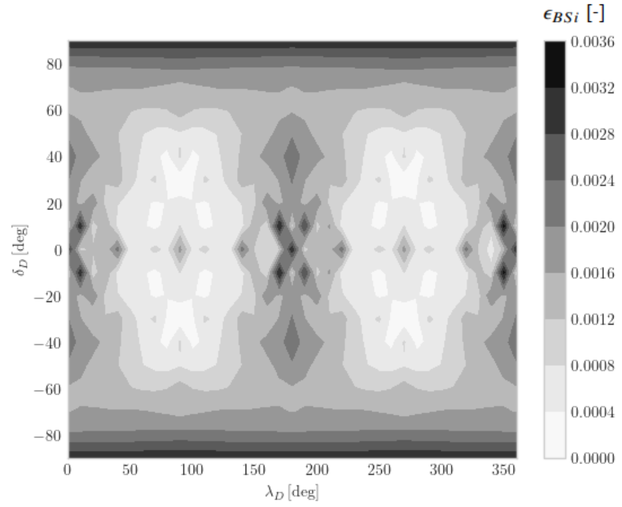

Figure 7: Relative error of MC acceleration with respect to the ABP acceleration on the Brillouin sphere in equirectangular projection on the example of Didymos

Table 5: Glossary of cases

	$\phi_0 = 0$	$\phi_0 = \pi/2$	$\phi_0 = \pi$	$\phi_0 = 3\pi/2$
$\Lambda_0 = 0$	case 1	case 5	case 9	case 13
$\Lambda_0 = \pi/2$	case 2	case 6	case 10	case 14
$\Lambda_0 = \pi$	case 3	case 7	case 11	case 15
$\Lambda_0 = 3\pi/2$	case 4	case 8	case 12	case 16

tude and longitude at latitudes of $\delta_i \in \langle -20°; 20° \rangle$ and $5°$ for latitudes of $\delta_i \in \langle -90°; -20° \rangle \cup \langle 20°; 90° \rangle$. The initial conditions on the surface that lead to levitation from rest are subjected to numerical propagation of the PDM equations of motion, which is then terminated upon crossing the BS or redeposition on the surface.

Numerical integration and termination conditions

All analyses of the dust particles' motion are conducted by means of numerical propagation of either the PDM or ABP equations of motion in the respective system. We use the Dormand-Prince integration scheme implemented in `SciPy` [50, 51] with the relative and absolute tolerances set to 10^{-13}. Alternative termination conditions of the propagation included crossing of the BS of Didymos, crossing of the BS of Dimorphos, and crossing of the Hill sphere of the binary system. All numerical propagations of the dust particle motion in this work follow the termination settings outlined in this section.

Results

In this section, results of the levitation analysis are presented. On the grid of 24840 nodes on the ellipsoid's surface, the number of nodes at which particles experience levitation is 7592 ± 4, depending between the initial conditions of the system. In addition, initial state vectors at the points of levitation (defined in the spherical body-fixed frame) differ negligibly between different starting conditions of the system, i.e., cases. Analogously, negligible differences were found for the results at the BS. This indicates that the centrifugal effect due to the rotation of Didymos is the primary factor determining levitation and all other effects may be treated as perturbations in the context of levitation. Taking into account significant similarities between the 16 cases, the results of the analysis are presented only for one of them, i.e., $\phi_0 = \pi$, $\Lambda_0 = 3\pi/2$.

Levitation from the surface of Didymos

Levitation from the primary takes place on a patterned region (see fig. 8). This is due to its regular shape in the dynamical model used in this paper, that the shape of the levitation region is closely related to the ellipsoidal shape model of Didymos. The red contour marks the boundaries of the levitation region. The bubble-shaped residual features of the red contour concentrated around certain longitudes are caused by smaller distance from the center of mass in these areas, since the y_D-axis-radius of the ellipsoid is smaller than any other on the equator plane, i.e., $a_D > b_D$. Therefore, the small red dots in fig. 8 constitute merely a visualization of an interpolation error and are neglected in the analysis.

Conditions at the Brillouin sphere

The propagation of initial state vectors at the points of levitation rendered 16 sets of position and velocity coordinates at the Brillouin sphere, one set for each case. None of the propagated trajectories resulted in redeposition on the surface of Didymos. Fig. 9 presents a map of particles in spherical coordinates in the Didymos-fixed frame, where the levitated particles were found to cross the BS. A comparison between fig. 8 and fig. 9 demonstrates that levitated particles insignificantly change their spherical coordinates in the Didymos-fixed frame (disregarding the radius r_D for obvious reasons) before reaching the BS. This observation may be explained by the short distance between the surface and the BS in the regions of levitation and large initial velocities at levitation, i.e., typically $v \approx 0.05\ \mathrm{m\,s^{-1}}$. As indicated in fig. 10, the longitudinal distribution of levitated particles at the BS is approximately constant, with minor increments in vicinity of the largest semi-axis of the ellipsoid,

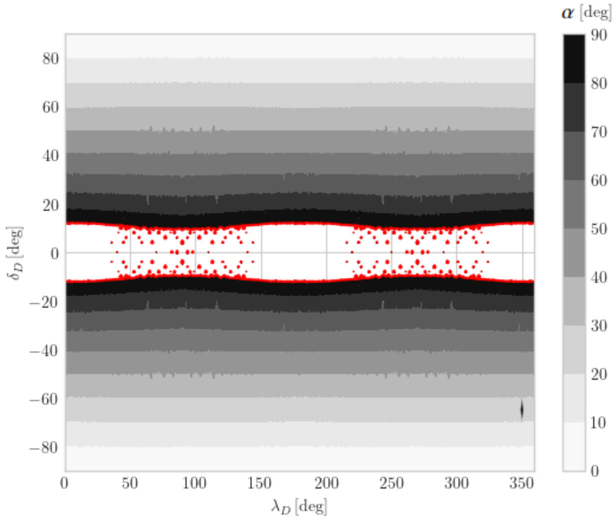

Figure 8: Experienced slope by particles resting on the surface of Didymos in equirectangular projection (example plot for $t = 0$, $\phi_0 = \pi$, $\Lambda_0 = 3\pi/2$); levitation regions are marked with white in red contour

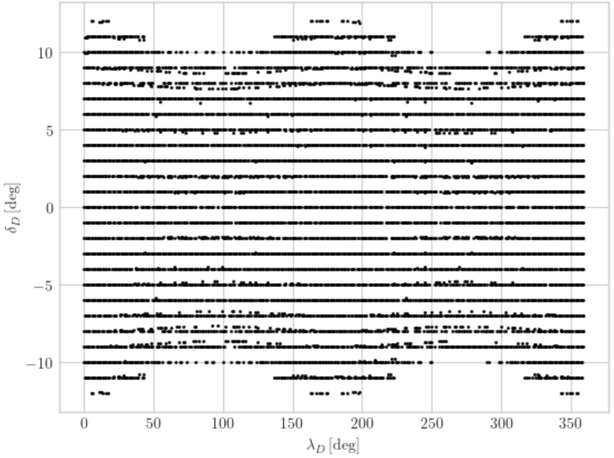

Figure 9: Location of propagated trajectories after levitation at the BS of Didymos in equirectangular projection (example plot for $t = t_{BS}$, $\phi_0 = \pi$, $\Lambda_0 = 3\pi/2$)

i.e., at $\lambda \in \{0, \pi\}$. In addition, the tangential velocity component (defined in the spherical body-fixed frame) dominates over the radial component at all longitudes (see fig. 11, which presents the interpolated magnitudes of normal and tangential components of the particles' velocity vector at the instant of levitation).

The result of this analysis is 16 sets of approximately 7600 state vectors at the BS of Didymos.

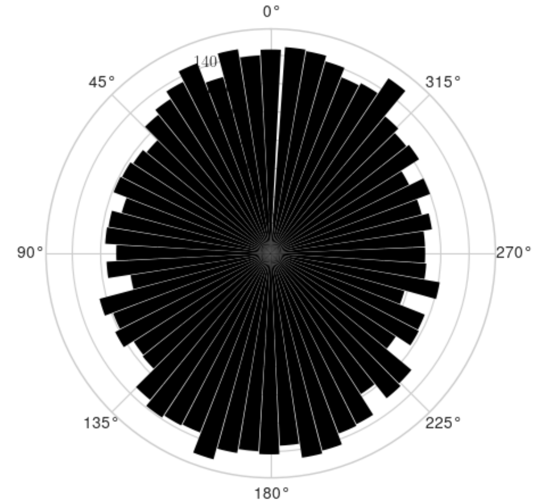

Figure 10: Longitudinal histogram distribution of the location of piercing the BS of Didymos after levitation (example plot for $t = t_{BS}$, $\phi_0 = \pi$, $\Lambda_0 = 3\pi/2$)

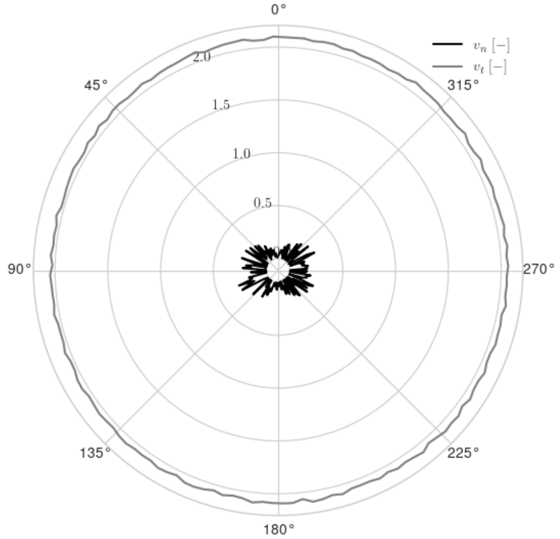

Figure 11: Longitudinal magnitudes of the normal (v_n) and tangential (v_t) velocities at the BS of Didymos after levitation (example plot for $t = t_{BS}$, $\phi_0 = \pi$, $\Lambda_0 = 3\pi/2$)

The results display significant consistency along the equator and negligible difference in distribution or direction of the velocity vector at the BS between the cases of the system's initial conditions.

Fates of levitated particles

To determine the fates of the levitated particles that cross the BS of Didymos, we propagate in ABP the conditions at the BS for the duration of $3T$. The fates of the levitated particles (see fig. 12, summarized in tab. 6) indicate small deviation of the numbers of survived particles n_s, particles collided with Didymos n_D, and particles collided with Dimorphos n_d. A strong sorting effect is seen in fig. 12, where a clear demarcation in regions is observed; particles levitated from a given region of the primary's surface meet a similar fate as the particles in its neighborhood. Approximately 60% levitated particles are subject to reaccretion in the equatorial regions of Didymos. About 30% of levitated particles survive for the propagation time of 15 days, which suggests an existence of a regolith dust cloud around the binary. Approximately 7% of levitated particles are subject to mass transfer to Dimorphos; however, only half of them are deposited on the Didymos-facing hemisphere of Dimorphos. We observe a strong dependence between the orientation of the primary Λ and the fraction of levitated particles that escape the binary system within the 15 days of propagation; for $\Lambda_0 \in \{\pi/2; 3\pi/2\}$, the fraction of escaping particles amounts about 1.5% of all levitated grains, whereas this figure is approximately 2-3 times smaller in other studied cases (i.e., $\Lambda_0 \in \{0; \pi\}$).

We observe strong sorting effect in the fates of levitating particles when the largest semi-axis of Didymos is parallel to the y-axis (even-numbered cases of fig. 12). To better understand the nature of the sorting phenomenon on the example of case 2, we study the fates of particles levitated from around longitudes of 180-200 degrees by tracing the trajectories after levitation for particles on a refined grid. As shown in fig. 13, which studies the fates of particles levitated on a refined grid on the surface of Didymos ($\lambda \in \{175^\circ, 175.1^\circ, \ldots, 214.9^\circ, 215^\circ\}$, $\delta = 0^\circ$), and in fig. 14, which presents a close-up view of the trajectories given in fig. 13 that pass in the vicinity of Dimorphos's BS, a sorting phenomenon is observed. We deem that it is a specific example of a gravity assist that redirects a stream of levitated particles on trajectories escaping from the binary system upon a close pass to the surface of Dimorphos. As seen in tab. 6, the occurrence of the sorting effect is correlated to the 2- to 3-fold increase in the percentage of the levitated particles escaping the binary. The levitated regolith particles from the refined-grid region that are re-deposited on Didymos are found to collide with the primary at all longitudes along the equator (see fig. 15). This observation, in the context of the numbers given in column n_D of tab. 6, strongly suggests a complex mechanism of approximately uniform (see fig. 19) regolith relocation in the equatorial regions, which effectively slows down the depletion of the regolith material of Didymos.

A similar observation can be made with regards to the dust particles transferred to Dimorphos; however, in this case the majority of transfer trajectories leads to deposition in the Didymos-facing hemisphere of Dimorphos, i.e., in the equatorial region between longitudes of 90° and 270° (see fig. 16). A similar flow of particles leading to mass transfer between the asteroids is observed in all studied cases, which implies a high probability of the occurrence of continuous, quasi-steady flow of dust, as observed in binary-star systems [52]. The topology of the trajectories presented in fig. 16 also indicate a mechanism of deposition of the regolith material levitated from Didymos on the non-Didymos-facing regions of Dimorphos. The percentages of the transferred particles per case that deposit on the outward-facing half of Dimorphos given in the n_d^* column of tab. 6 suggest that approximately 50-60% of the Didymos-Dimorphos transferred particles deposit on the outward-facing facet of Dimorphos.

One trajectory of each fate of levitated particles is plotted in fig. 17 to present examples of the trajectory topologies. As observed in fig. 17 in the demonstrated 'survived' case, some levitated particles follow intricate trajectories, as further demonstrated in fig. 18.

Regions of stable motion: This section discusses the methodology adopted to identify regions of stable motion in the Didymos system. First, the problem of periodicity in a non-autonomous dynamical system is analyzed. Then, the grid search approach is discussed along with the results thereof.

Periodicity

The ABP describes a non-autonomous system due to the time-dependency (in $\mathcal{F}$) of the primary's gravity field, the SRP acceleration and the third-body effect. Therefore, orbital motion in the system under analysis can only be periodic when it is aligned with the synodic periods (in $\mathcal{F}$) of the motion of the Sun and the rotation of Didymos. The synodic rotation rate of the primary is given, analogous to eq. 8, as

$$\Omega_D = \left(T_b^{-1} + T_D^{-1}\right) T_b \,, \tag{24}$$

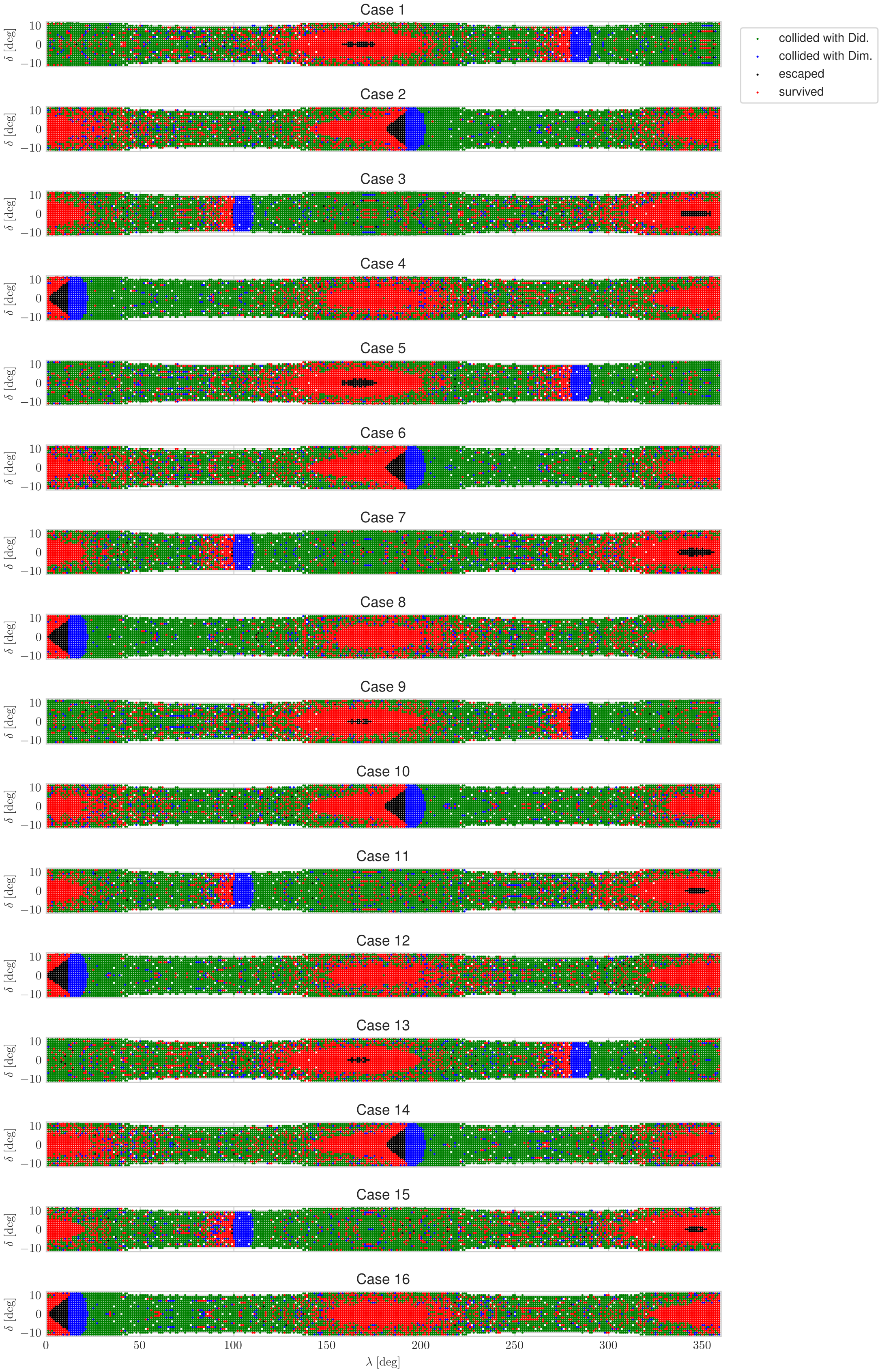

Figure 12: Fates of the levitated particles after a propagation for $3T$ after crossing the BS of Didymos

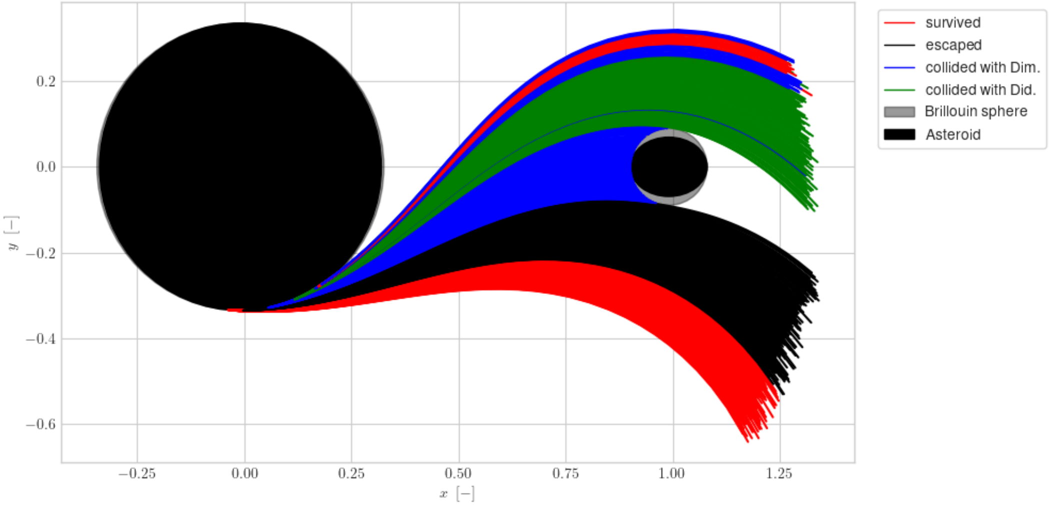

Figure 13: Trajectories of the levitated particles on the refined sub-grid in the region of the strong sorting occurrence

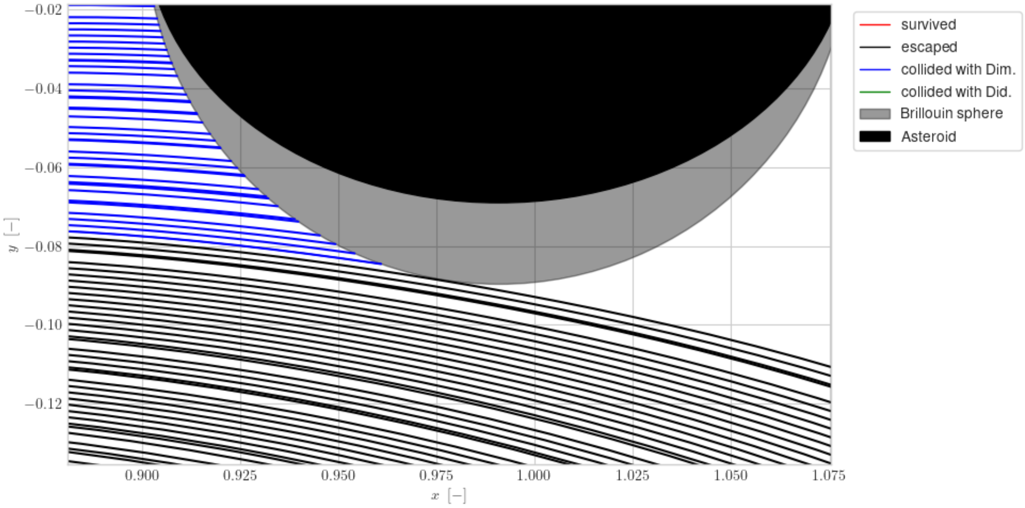

Figure 14: Trajectories closely missing Dimorphos leading to escape from the binary

whereas the synodic period of the Sun's motion and Didymos' rotation is defined, respectively, as

$$(T_s)_{\mathcal{F}} = T_s \, Q_s \tag{25}$$

$$(T_D)_{\mathcal{F}} = T_D \, Q_D \; . \tag{26}$$

Tab. 7 lists the smallest common multiples of the two synodic periods. The periods were assumed to be within the tolerances specified in tab. 3 and tab. 1. Since the period of the heliocentric orbit of the binary $\underline{T}_h$ is approximately 770 days, we consider only the smallest value presented in tab. 7 for the analysis; if larger periods were analyzed, the assumed constant magnitude of the SRP perturbation in the ABP would introduce large errors in the results due to the large eccentricity of the binary's heliocentric orbit.

Grid search

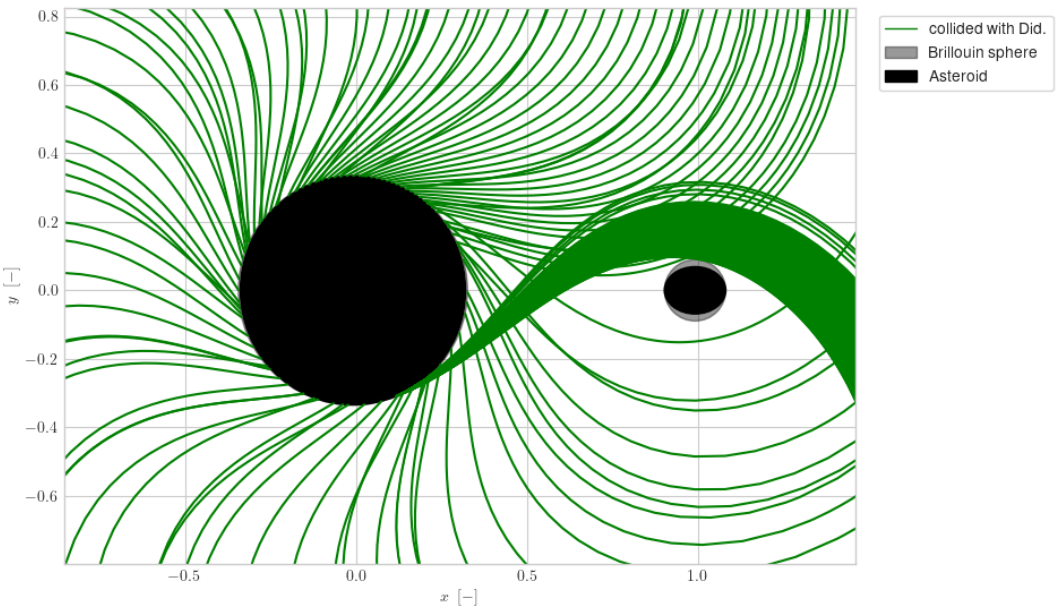

Figure 15: Trajectories leading to dust reaccretion on the surface of Didymos (in the refined grid analysis)

Table 6: Statistics of the fates of levitated particles
(N_{total} - total number levitated particles, n_s - fraction of particles that survived, n_D - fraction of particles that collided with Didymos, n_d - fraction of particles that collided with Dimorphos, n_d^* - fraction of particles that collided with Dimorphos' non-Didymos-facing hemisphere)

Case number	ϕ_0	Λ_0	N_{total}	n_s	n_D	n_d	n_d^*	n_e
1	0	0	7592	28.09%	63.99%	7.17%	3.54%	0.75%
2	0	$\pi/2$	7588	31.51%	59.83%	7.26%	3.61%	1.40%
3	0	π	7592	28.54%	63.51%	7.09%	3.65%	0.85%
4	0	$3\pi/2$	7588	31.80%	59.70%	7.05%	3.44%	1.45%
5	$\pi/2$	0	7596	27.07%	64.65%	7.37%	3.78%	0.91%
6	$\pi/2$	$\pi/2$	7590	30.84%	60.50%	7.11%	3.49%	1.54%
7	$\pi/2$	π	7596	26.95%	64.47%	7.56%	3.98%	1.01%
8	$\pi/2$	$3\pi/2$	7590	30.95%	60.43%	7.06%	3.43%	1.55%
9	π	0	7596	26.90%	65.46%	7.28%	3.44%	0.47%
10	π	$\pi/2$	7588	29.65%	61.66%	7.09%	3.41%	1.59%
11	π	π	7596	25.99%	66.13%	7.29%	3.55%	0.59%
12	π	$3\pi/2$	7588	29.78%	61.54%	7.04%	3.26%	1.63%
13	$3\pi/2$	0	7596	26.97%	64.81%	7.70%	4.25%	0.51%
14	$3\pi/2$	$\pi/2$	7590	30.79%	60.30%	7.39%	3.83%	1.51%
15	$3\pi/2$	π	7596	26.80%	65.03%	7.58%	4.05%	0.58%
16	$3\pi/2$	$3\pi/2$	7590	30.88%	60.34%	7.29%	3.61%	1.49%

Due to the time-dependent nature of the problem at hand and the clearly defined targeted period of the sought solution, a period-constrained differential correction scheme given by Heiligers et al. [53] was analyzed for its performance when applied to the problem of this work. However, due to

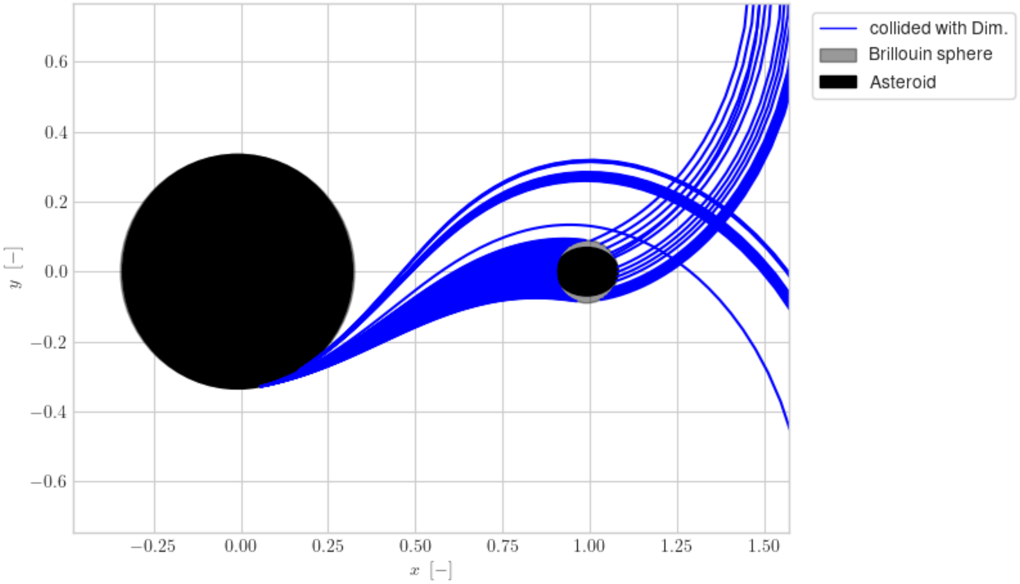

Figure 16: Trajectories leading to dust re-deposition on the surface of Dimorphos (in the refined grid analysis)

Table 7: Periods asserting true periodicity in the Didymos system

Period T ($\underline{T}$)	Multiple of $(T_D)_{\mathcal{F}}$	Multiple of $(T_S)_{\mathcal{F}}$
69.07 (5 d 11.00 h)	47	11
301.46 (23 d 19.75 h)	205	48
370.57 (29 d 6.83 h)	252	59
672.03 (53 d 2.57 h)	457	107
741.14 (58 d 13.66 h)	504	118

the multiple-revolution topology of all of the candidate trajectories to be optimized using said correction scheme, this single-shooting method was incapable of reaching convergence. We selected the conventional grid search technique to ensure non-diverging behavior of the optimization algorithm; however, we recommend investigating the performance of multiple-shooting methods to attempt an improvement in the computational efficiency of the periodic-orbit search.

We use a classical grid search technique to identify initial conditions that lead to quasi-periodic solutions [54]. The search is divided into two stages: coarse and refined. The coarse search studies the entirety of the discretized search domain (see tab. C1) via propagating the initial conditions over a time span T in the ABP model. Around the nodes in the grid search where $\|\mathbf{x}(t=0)-\mathbf{x}(t=T)\| \leq 0.1$ (see tab. 8), a refined grid search is performed (the discretization around these nodes is outlined in tab. C2). By lowering the constraint on the Euclidean norm of the distance between the initial and final conditions in the refined search to 0.01, only two sets of initial conditions for quasi-satellite orbits (QSO) and two for distant retrograde orbits (DRO) trajectories were found to satisfy the condition (see tab. 9 and their visual representation respectively in fig. 20). The presented refinement of the domain resulted in an improvement of the solutions by a factor of 2 and 5 (see tab. 8), respectively to the DO and QSO, and may be performed iteratively to further improve the precision of the solutions. The search has been performed for $\phi_0 = \Lambda_0 = 0$.

Temporary capture: This section introduces the approach adopted to identify trajectories of the levitated regolith particles leading to temporary capture in the discovered bounded-motion trajectories. The results are discussed in the context of a mission risk analysis for the Hera spacecraft.

Methodology

Temporary capture of levitated particles may occur if the escape trajectory (in the state space sense) passes close to a trajectory identified as a periodic orbit [55]. The flow of the state space

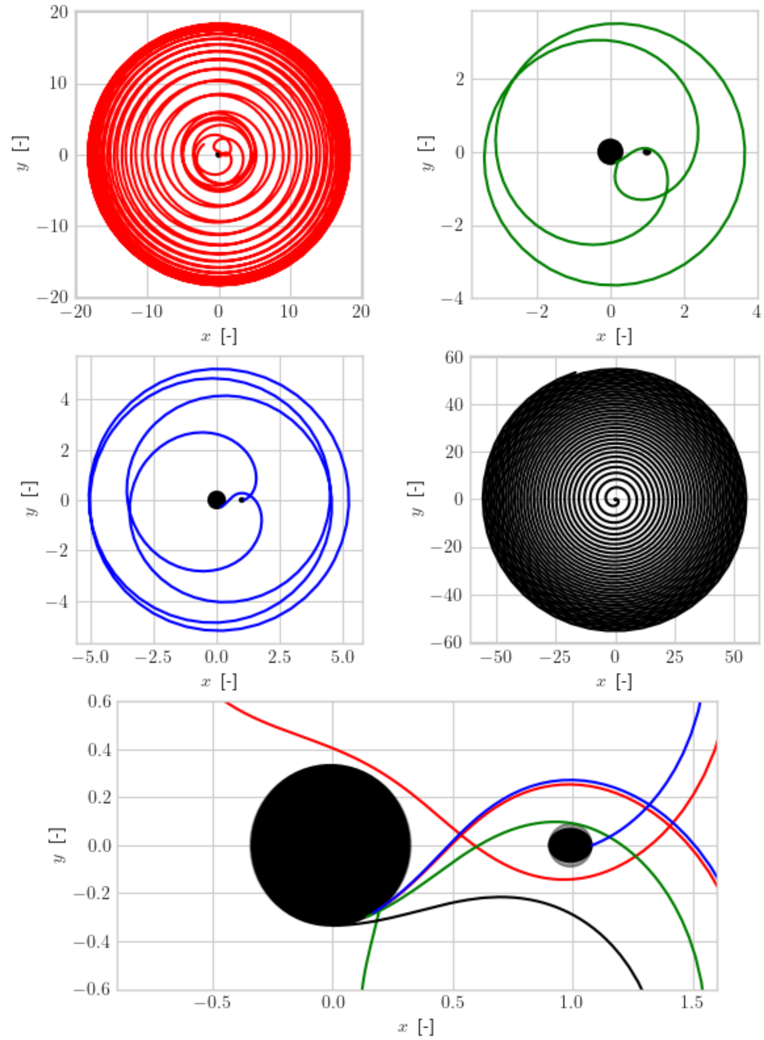

Figure 17: Examples of topology of trajectories for each of the four fates of the levitated particles (labelling analogous to the one found in fig. 12 and fig. 13)

is not stationary due to the non-autonomous character of the problem; hence, the conventional 6-element state space does not represent all degrees of freedom of the problem. We expand the state space by two additional dimensions: the orientation of the primary Λ and the angular position of the third body in the bicircular problem ϕ. Hence, we effectively freeze the flow and may treat it as stationary in the eight-dimensional state space, which will be referred to as the 'augmented state space' $\mathbf{D}$ and a point in that space as an 'augmented state vector' $\mathbf{X}$.

Since virtually all temporary capture trajectories are anticipated to be composed of two segments of non-zero length, i.e., a propagated levitation trajectory originating at the surface and a trajectory constituting part of the periodic orbit, they are referred to as the levitation and orbital segments of the temporary capture trajectory. These trajectories are denoted as $C_{\mathbf{x}_l}$ and $C_{\mathbf{x}_o}$, respectively (see

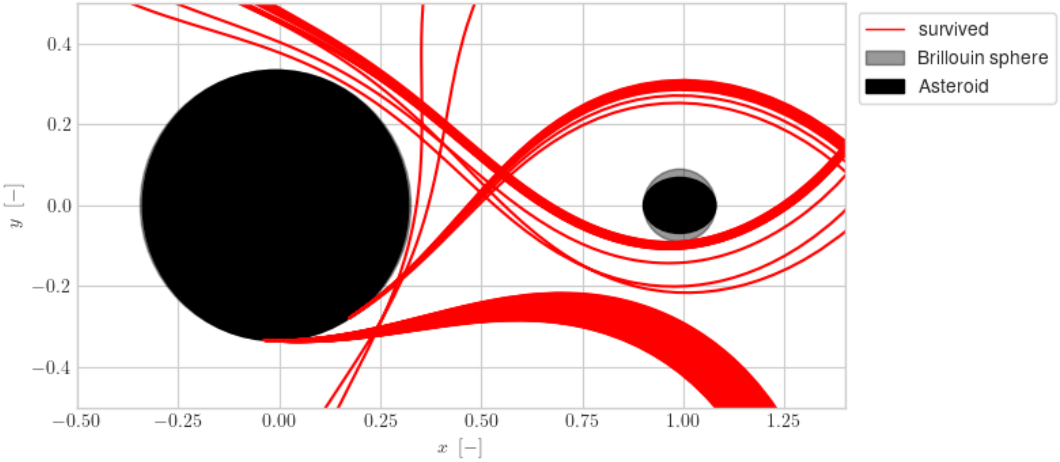

Figure 18: Trajectories of 'survived' levitated particles from the refined analysis in the vicinity of the primaries

Table 8: Overview of the coarse and refined grid search results

Stage	No. of nodes	Threshold value of $\|\mathbf{x}(t=0)-\mathbf{x}(t=T)\|$	No. of solutions	Smallest value of $\|\mathbf{x}(t=0)-\mathbf{x}(t=T)\|$
DO				
Coarse	16335	0.1	15	0.0145
Fine	17760	0.01	2	0.0073
QSO				
Coarse	20700	0.1	23	0.0271
Fine	54450	0.01	2	0.0054

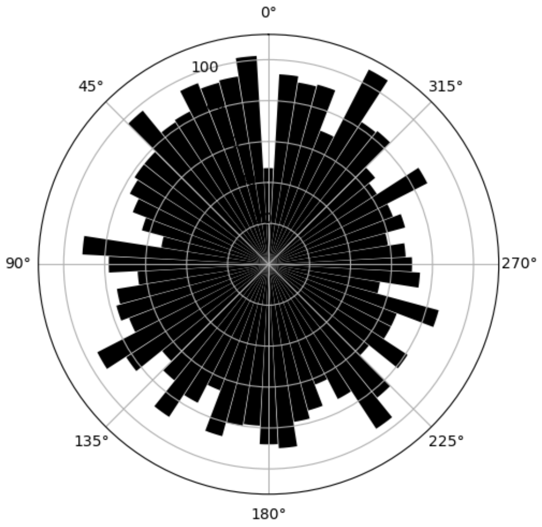

Figure 19: Longitudinal histogram distribution of piercing the BS of Didymos at redeposition (example plot for $t=t_{BS}$, $\phi_0=\pi$, $\Lambda_0=3\pi/2$)

eq. 27). The occurrence of temporary capture is determined by finding the capture error, i.e., the minimum distance d^* between the levitation and orbital trajectories in $\mathbf{D}$. Effectively, this procedure consists in calculating the sum of three Euclidean distance matrices using the distance operator d [56], of which the minimum off-diagonal element is the result of the operation

$$d^*(C_{\mathbf{X}_l}, C_{\mathbf{X}_o}) = \\ = \min_{\mathbf{X}_l\in C_{\mathbf{X}_l}, \mathbf{X}_o\in C_{\mathbf{X}_o}} \left(d(\mathbf{x}_l,\mathbf{x}_o)+d(\mathbf{\Lambda}_l,\mathbf{\Lambda}_o)+d(\boldsymbol{\phi}_l,\boldsymbol{\phi}_o)\right) \tag{27}$$

where $\boldsymbol{\phi}$ and $\mathbf{\Lambda}$ are the corresponding state history vectors of ϕ and Λ.

Discussion of results

Tab. 10 gives an overview of the minimum temporary capture errors for the selected orbits. The results obtained for QSO1 and QSO2 indicate the smallest capture error at $t=0$, i.e., at piercing the BS upon levitation, which is not the case for DO1

Table 9: Solutions of the grid search

ID	$\mathbf{x}(t=0)$ $[-]$	$\lVert\mathbf{x}(T)-\mathbf{x}(0)\rVert$ $[-]$	$\lVert\underline{\mathbf{r}}(T)-\underline{\mathbf{r}}(0)\rVert$ $[\mathrm{m}]$	$\lVert\dot{\underline{\mathbf{r}}}(T)-\dot{\underline{\mathbf{r}}}(0)\rVert$ $[\mathrm{cm/s}]$
DO1	$[-1.68417602,\ 0,\ 0.024,\ 0.02,\ 2.56152879,\ 0]^T$	0.00731	5.435	0.016
DO2	$[-1.68417602,\ 0,\ 0.03,\ -0.1,\ 2.55597323,\ 0]^T$	0.00769	4.638	0.018
QSO1	$[-0.52096283,\ 0,\ 0,\ 0,\ 1.91061955,\ 0]^T$	0.00537	2.380	0.014
QSO2	$[-0.52096283,\ 0,\ 0,\ 0.005,\ 1.91061955,\ 0]^T$	0.00947	5.071	0.023

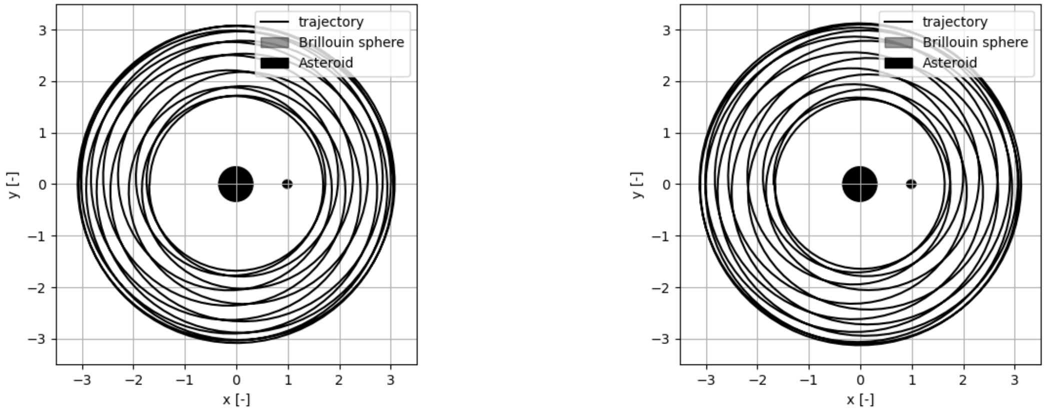

(a) DO1

(b) DO2

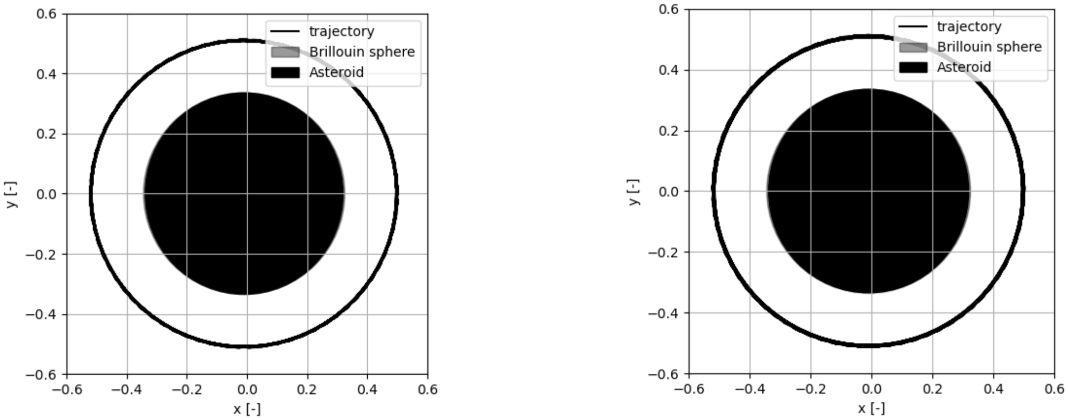

(c) QSO1

(d) QSO2

Figure 20: Trajectories of DO1, DO2, QSO1, and QSO2 in the x-y plane of $\mathcal{F}$

and DO2. The capture errors found in the analysis are large, where the largest contributing factor is the error in the state vector. The smallest capture error was found for the DO1 orbit, which amounts for 0.3276 error in position (equivalent to 389.84 m) and 0.3858 in velocity (corresponding to 1.056 cm/s). We anticipate two possible reasons for such magnitudes of capture errors. First, the distance calculated using eq. 27 does not account for different weights given to various components of the augmented state vector. Another factor that might result in reduced accuracy of the identified temporary capture trajectories is the discretization of the trajectory. Eq. 27 identifies the closest pair-wise distance between individual (augmented) state vectors but does not account for the fact that the studied trajectories are continuous.

Since the smallest capture error for the QSOs is significantly larger than those for the DO case and corresponds to the instant of levitation of the particles, we consider only the DO temporary capture cases for further discussion. The distribution of capture errors on the surface of Didymos (see fig. 22) does not render any trivial correlation between the levitation coordinates, the system state variables, and the capture error magnitude. As shown in the trajectory plot of the best solution (characterized by the smallest $d(C_{\mathbf{X}_l}, C_{\mathbf{X}_o})$) given in fig. 21, the two trajectories do not appear to be close to intersecting. Therefore, the results are not sufficient to formulate conclusions with regards to the feasibility or infeasibility of temporary capture of off-Didymos-levitated regolith particles into periodic orbits in the binary system.

In light of the large capture errors, in particular in the case of QSOs, for further research we recommend restricting the set of orbits considered for possible temporary capture by studying only orbits of similar orbital energy amplitudes as the levitated particles. The analysis could be further improved by interpolation of the trajectory (or, to preserve computational resources, only selected segments where trajectories pass in close vicinity to one another). Then, the distance could be found analytically, i.e., through solving a system of eight differential equations derived from the squared difference of the two interpolated trajectory segments $(\tilde{C}_{\mathbf{X}_l} - \tilde{C}_{\mathbf{X}_o})^2$, or numerically, e.g., by refining the discretization of the trajectories used in eq. 27.

Regions of increased Hear-regolith collision risk

Assessment of the threat posed by the regolith particles to a spacecraft visiting the binary system is conducted by first analyzing all findings of this work to identify trends in long-timescale motion of the dust grains and, subsequently, quantitatively investigating these phenomena. First, the primary region of hazard to the spacecraft would be the vicinity of the invariable plane of the system due to the small latitudes of levitated conditions and given the symmetry in the z-axis of the ABP and PDM. The discussions given in section and section 'Discussion of results' suggest three types of regolith particle trajectories that might be of significant hazard to a spacecraft performing *in situ* observations in the Didymos system, such as Hera: (1) levitated trajectories destined to escape the binary (in short, "escaping" trajectories), as their slow motion toward the Hill Sphere would create a disk of regolith orderly moving outwards of the binary system in an orderly manner, (2) chaotic, non-periodic survived trajectories of particles levitated from Didymos ("chaotic" trajectories), as they tend to remain within the binary for extended periods of time ($3T$ corresponds to a time span longer than 15 days), and (3) levitated particles captured into periodic orbits ("captured" trajectories) due to their inherently very extended times of deposition in orbit (in theory, such particles should be in their orbits for infinite time periods).

The escaping trajectories are included in the glossary of risk-posing trajectories due to their extended travel time from levitation to crossing the Hill Sphere. Escape trajectories of travel time beyond 15 days have been identified in the analysis given in section . This observation, in light of the uncertain levitation rate from Didymos due to a lack of *in situ* studies, renders a possible scenario of a deadly dust disk surrounding the binary system which slowly spirals outwards and ultimately escapes its sphere of influence. The chaotic trajectories, similar as in the case of escaping trajectories, pose significant threat to a probe in the binary system due to the large uncertainty in their orbital lifetime. The captured trajectories, i.e., levitation trajectories that smoothly transition into perfect periodic orbits, (in theory) have a infinite orbital lifetime; however, given all dynamical perturbances not accounted for in this study, such solutions are inherently unstable and existence of such trajectories must be proven by *in situ* studies. Trajectories found in this research (such as in fig. 21) constitute a solid stepping stone for further refinement of the results, although we do not yet deem them of satisfactory precision to draw conclusions for high-fidelity mission planning of the Hera spacecraft.

As given in tab. 6, the levitation analysis showed that the survival rate after a time $3T$ of the levitated particles is 16-68 times larger than the escape rate. Accounting for the regions of motion of the two types of fates of the levitated particles (for an example refer to fig. 17), we anticipate two dust disks to exist around the binary system: (1) the outer disk is composed of regolith particles that follow escaping trajectories; the dust grains can be found as far as the Hill Sphere, their motion is highly ordered, and an approximately uniform density in the disk is expected, whereas (2) the inner disk spans as far as 20 km from the barycenter of the binary, motion of particles is chaotic, which suggests an existence of both time- and spatial fluctuations of the disk density. The ultimate fate of the inner-disk trajectories is likely a collision with one of the asteroids; however given the small escape rates of

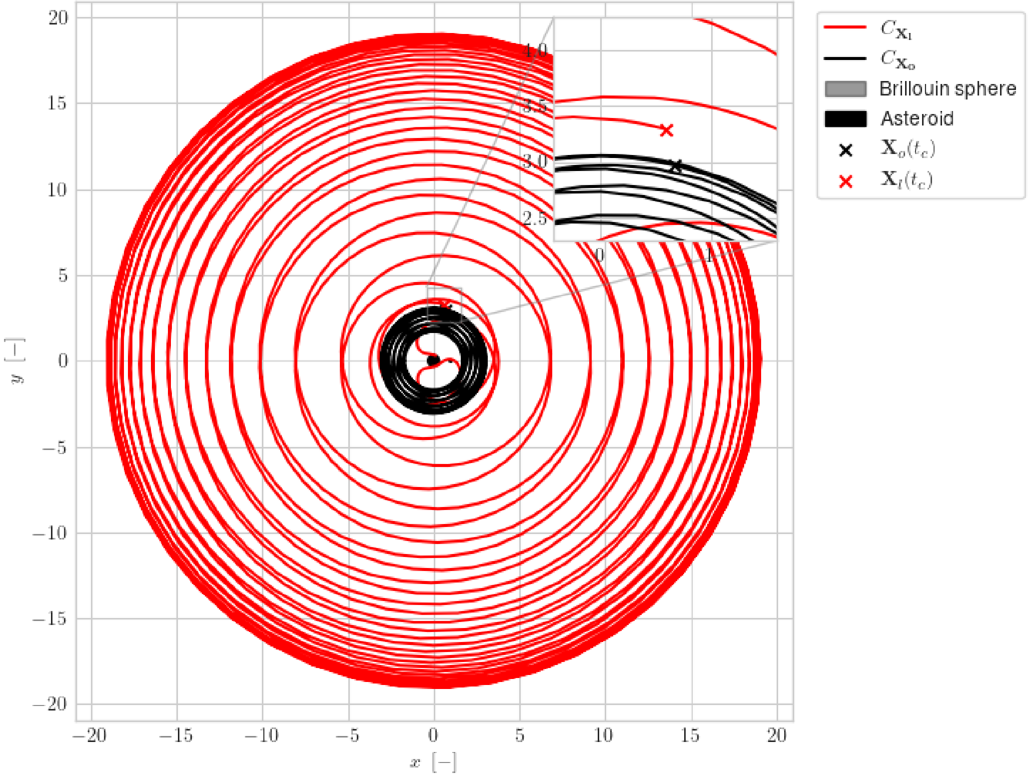

Figure 21: Plot of the levitation and periodic orbit trajectories of the smallest capture error case (DO1)

Table 10: Temporary capture results (* - the units for $d(\Lambda_l(t_c), \Lambda_o(t_c))$ and $d(\phi_l(t_c), \phi_o(t_c))$ are dropped in eq. 27.)

Orbit ID	Lev. case	$d^*(C_{\mathbf{X}_l}, C_{\mathbf{X}_o})$ [-]*	$d(\Lambda_l(t_c), \Lambda_o(t_c))$ [rad]	$d(\phi_l(t_c), \phi_o(t_c))$ [rad]	$d(\mathbf{x}_l(t_c), \mathbf{x}_o(t_c))$ [-]
QSO1	1	0.85421	0	0	0.85421
QSO2	1	0.85436	0	0	0.85436
DO1	8	0.52864	0.00087	0.02160	0.50617
DO1	6	0.58766	0.01207	0.03886	0.53673

the dust from the system after levitation, the regolith relocation mechanism proposed in section 'Fates of levitated particles', and the long orbital lifetimes of the inner-disk trajectories, we anticipate that the inner disk is an ever-changing, dynamic, and self-exciting dust cloud spanning 20 km from the barycenter of the system in the invariable plane and up to 80 m in the normal-to-invariable-plane direction. Nevertheless, due to the uncertainties related to the properties of the asteroids of the Didymos binary, it is impossible to assess the densities of the two dust disks without the *in situ*-collected information about the levitation mass flow off Didymos, which the DART-accompanying probes might soon deliver [7].

Conclusion: In this paper, motion of superficial regolith particles levitated from Didymos, the primary body of the Didymos binary asteroid system, has been studied in order to identify regions of elevated risks for the Hera spacecraft. The work has been divided into three major stages: (1) analysis of levitation of the superficial boulders of 5 cm in diameter, which also included numerical propagation of the trajectories to determine their fates, (2) grid searches for periodic orbits in the vicinity of the invariable plane of the system, and (3) based on the results of the former stages to determine whether the levitation of dust particles may lead to temporary capture in a periodic orbit.

The employed high-fidelity dynamical model enabled exposing numerous intricacies of the behavior of levitated regolith grains. Iterative grid searches allowed to identify four periodic orbits under the imposed tolerance: two distant retrograde orbits, i.e., revolving around the binary system, and two quasi-satellite orbits, i.e., revolving around the primary body, Didymos. Analysis of the orbital evolution of trajectories originating upon levitation from the primary body, Didymos, resulted in a comprehensive overview of the behavior of the loose regolith from the equatorial regions of Didymos. Approximately 60% of the levitated particles were found to redeposit on Didymos within 15 days of levitation, whereas 7% of the levitated particles collide with the secondary body, Dimorphos. The rate of collision with Dimorphos is approximately equal between the Didymos- and outer space-facing hemispheres of the tidally-locked moonlet. One of the most important takeaways of the study is the discovery of escape of a relatively large portion of the levitated particles (about 1%) through a sorting mechanism, i.e., ejection of the particles outside the Hill Sphere of the binary system after close encounter with Dimorphos. Almost 30% of the levitated trajectories remain in the binary system (do not escape and do not deposit on any of the asteroids) after the propagation period slightly exceeding 15 days; prominent existence of dust ejecta clouds in the Didymos system months after the DART spacecraft's impact indicate that the survival periods might be much longer than the 15 days which constituted the propagation limit in the study. The phenomena of extended survival in the binary system and slow, spiraling escape from the system suggest existence of a very polluted (in the sense of the regolith) regions throughout the binary system, in the vicinity of its invariable plane. Existence of two dust disks has been suggested as potential region of elevated hazard for the visiting spacecraft. Temporary capture of particles in periodic orbits in the binary system has not been demonstrated due to large capture errors (the smallest approach between two trajectories - one levitation and one periodic trajectory - was found to be characterized by a position error of approximately 400 m and a velocity error of above 1 cm/s).

The findings are anticipated to render important contributions to planning of the Hera spacecraft's operations in the Didymos system and to provide a valuable starting point for further investigation of the dust dynamics in said system. We deem the demonstrated methodology applicable for studying the dynamics of particles larger than 0.1 µm, as below this threshold the motion of regolith particles is dominated by the effects of electrostatic forces [57]. The study was based on several assumptions, such as the assumption of planar motion of the Sun around the binary, constant distance to the Sun, and simplified shapes of the primaries. Moreover, a range of diameters of particles under consideration could be expanded and applying multiple-shooting methods for identifying periodic orbit could be investigated. Furthermore, the recent arrival of the DART probe to the binary is expected to deliver much more detailed data on the binary and remove numerous uncertainties pointed out in this work.

References: [1] Planetary Science Communications, Jet Propulsion Laboratory, NASA (2022) Apophis accessed on: 27-11-2022. [2] L. A. McFadden, et al. (2006) *Near-Earth Objects* Gale virtual reference library Elsevier Science ISBN 9780080474984. [3] R. Dymock (2010) *Asteroids and Dwarf Planets and How to Observe Them* Astronomers' Observing Guides Springer New York `doi`. [4] D. P. S. Dearborn, et al. (2015) *Defending Against Asteroids and Comets* Handbook of Cosmic Hazards and Planetary Defense Springer International Publishing `doi`. [5] A. F. Cheng, et al. (2018) *Planetary and Space Science* 157(November 2017):104 ISSN 00320633 `doi`. [6] P. Michel, et al. (2016) *Advances in Space Research* 57(12):2529 `doi`. [7] P. Michel, et al. (2018) *Advances in Space Research* 62(8):2261 ISSN 18791948 `doi`. [8] Planetary Science Communications, Jet Propulsion Laboratory, NASA (2022) Didymos & Dimorphos accessed on: 27-11-2022. [9] Safety & Security, European Space Agency (2020) Hera, Bonus Science accessed on: 20-11-2020. [10] A. F. Cheng, et al. (2020) *Icarus* 352(November 2019):113989 ISSN 10902643 `doi`. [11] Y. Zhang, et al. (2017) *Icarus* 294:98 ISSN 10902643 `doi`. [12] Y. Yu, et al. (2018) *The Astronomical Journal* 156(2):59 ISSN 0004-6256 `doi`. [13] Y. Yu, et al. (2018) *Icarus* 312:128 ISSN 10902643 `doi`.`arXiv:1708.00592`. [14] Y. Yu, et al. (2019) *Monthly Notices of the Royal Astronomical Society* 484(1):1057 ISSN 13652966 `doi`. [15] P. Sánchez, et al. (2019) *Icarus* 338(September) ISSN 10902643 `doi`.`arXiv:1909.11270`. [16] D. J. Scheeres (2015) *Icarus* 247:1. [17] F. Ferrari, et al. (2018) *Advances in Space Research* 62(8):2245. [18] T. C. Oliveira, et al. (2020) *Revista Mexicana de Astronomia y Astrofisica* 56(1):113 ISSN 01851101 `doi`. [19] A. Capannolo, et al. (2019) *Journal of*

Guidance, Control, and Dynamics 42(1):189 ISSN 15333884 `doi`. [20] I. Jean, et al. (2019) *Journal of Guidance, Control, and Dynamics* 42(6):1319 ISSN 15333884 `doi`. [21] L. Dell'Elce, et al. (2017) *Advances in Space Research* 59(5):1304. [22] R. Lasagni Manghi, et al. (2018) *Advances in Space Research* 62(8):2290 ISSN 18791948 `doi`. [23] J. B. Silva Neto, et al. (2018) *Space Flight Mechanics Meeting, 2018* (210009) `doi`. [24] Y. Yu, et al. (2017) *Icarus* 282:313 ISSN 10902643 `doi`. [25] P. Wiegert (2020) *The Planetary Science Journal* 1(1):3 ISSN 2632-3338 `doi`. `arXiv:1912.09496`. [26] A. Fujiwara, et al. (2006) *Science* 312(5778):1330. [27] D. Lauretta, et al. (2019) *Science* 366(6470). [28] S. Watanabe, et al. (2019) *Science* 364(6437):268. [29] Solar System Dynamics, Jet Propulsion Laboratory, NASA (2020) 65803 Didymos (1996 GT) accessed on: 23-11-2020. [30] P. Pravec, et al. (2003) 8244:2. [31] P. Pravec, et al. (2006) *Icarus* 181(1):63. [32] S. P. Naidu, et al. (2020) *Icarus* 348(March):113777 ISSN 10902643 `doi`. [33] H. Agrusa, et al. (2020) in *AAS/Division for Planetary Sciences Meeting Abstracts* vol. 52 217–04. [34] European Space Research and Technology Centre (2014) . [35] F. Damme, et al. (2017) *Planetary and Space Science* 146:1. [36] H. F. Agrusa, et al. (2020) *Icarus* 349(January) ISSN 10902643 `doi`. [37] D. Richardson, et al. (2016) *LPI* (1903):1501. [38] P. Scheirich, et al. (2009) *Icarus* 200(2):531. [39] J. Heiligers, et al. (2018) *Journal of Guidance, Control, and Dynamics* 41(9):1947. [40] V. Szebehely (1967) Theory of orbits: the restricted three body problem. [41] W. Koon, et al. (2006) *The Three-Body Problem, and Space Mission Design (Pasadena, CA, USA: California Institute of Technology)*. [42] D. J. Scheeres (2016) Orbital motion in strongly perturbed environments: applications to asteroid, comet and planetary satellite orbiters. [43] Z. Li, et al. (2019) *Advances in Space Research* 63(3):1347. [44] C. R. McInnes (2004) *Solar sailing: technology, dynamics and mission applications* chap. 2. Solar radiation pressure Springer Science & Business Media. [45] D. Villegas Pinto, et al. (2020) *AIAA Scitech 2020 Forum* 1 PartF:1 `doi`. [46] S. S. Liew, et al. (2016) *Neurocomputing* 216:718. [47] X. Yang, et al. (2018) *Mathematical Problems in Engineering* 2018. [48] D. J. Scheeres (2012) *Celestial Mechanics and Dynamical Astronomy* 113(3):291 ISSN 09232958 `doi`. [49] S. Soldini, et al. (2020) *Planetary and Space Science* 180(September 2019):104740 ISSN 00320633 `doi`. [50] E. Jones, et al. (2016) Scipy: Open source scientific tools for python. [51] E. Hairer, et al. (1993) *Berlin, Germany*. [52] V. Nazarenko, et al. (2001) *Astronomy Reports* 45(6):452. [53] J. Heiligers, et al. (2016) *Astrophysics and Space Science* 361(7):1. [54] Y. Shi, et al. (2019) *Acta Astronautica* 163(July 2018):11 ISSN 00945765 `doi`. [55] D. J. Scheeres, et al. (2000) *Astronomy and Astrophysics* 356(2):747 ISSN 00046361. [56] G. Weyenberg, et al. (2015) in *Algebraic and Discrete Mathematical methods for modern Biology* 293–319 Elsevier. [57] J. R. Szalay, et al. (2018) *Dust Phenomena Relating to Airless Bodies* vol. 214 Springer Nature B.V. ISBN 1121401805 `doi`.

Appendix: Frame transformations: Transformation of position vectors is explained using the example of the Didymos-fixed frame ('D' index); however, the same relations hold for the Dimorphos-fixed one ('d' index). The transformation of the position vector between the Didymos-fixed ($\mathcal{F}_D$) and the synodic ($\mathcal{F}$) frame is given by

$$\mathbf{r} = \mathbb{R}_{D,s}(\Lambda_D)\mathbf{r}_D + \mathbf{T}_{D,s} \tag{28}$$

where $\mathbb{R}_{D,s}(\Lambda_D)$ and $\mathbf{T}_{D,s}$ are the Didymos-fixed-to-synodic rotation matrix by the Didymos's angle of rotation Λ_D (since the system is semi-asynchronous, $\Lambda_d = 0$) and the Didymos-fixed-to-synodic translation vector, respectively given by

$$\mathbb{R}_{D,s}(\Lambda_D) = \begin{bmatrix} \cos(\Lambda_D) & -\sin(\Lambda_D) & 0 \\ \sin(\Lambda_D) & \cos(\Lambda_D) & 0 \\ 0 & 0 & 0 \end{bmatrix} \tag{29}$$

$$\mathbf{T}_{D,s} = \mathbf{r}_D \tag{30}$$

The opposite transformation is defined as

$$\begin{aligned} \mathbf{r}_D = \mathbb{R}_{s,D}(\Lambda_D)\,[\mathbf{r} + \mathbf{T}_{s,D}] = \\ = \mathbb{R}^{-1}_{D,s}(\Lambda_D)\,[\mathbf{r} - \mathbf{T}_{D,s}] = \\ = \mathbb{R}^{T}_{D,s}(\Lambda_D)\,[\mathbf{r} - \mathbf{r}_D] \end{aligned} \tag{31}$$

Appendix: Eclipse model: To determine the lighting condition at a specific point, we derive the radius of the ellipsoid as seen from the perspective of the third body, i.e., projected on a plane normal to $\hat{\mathbf{S}}$. We define the eclipse reference frame of Didymos (however, the same approach is used for Dimorphos) $\mathcal{F}_{e_D}$ with the origin at the center of mass of Didymos, the x_{e_D}-axis points in the direction of $\hat{\mathbf{S}}$, the z_{e_D}-axis is aligned in the direction of z and the y_{e_D} completes the orthonormal system $\mathcal{F}_{e_D}(x_{e_D}, y_{e_D}, z_{e_D})$. The equation of an ellipse rotated by $\alpha_{e_D} = \Lambda_D - \phi$, i.e., the x_{e_D}-y_{e_D} projection of the ellipsoid's equator ($\delta_D = 0$, $r_D(\lambda_D, \delta_D) = r_{ell_D}(\lambda_D, \delta_D)$) in $\mathcal{F}_{e_D}$ (as in fig. 23) is

$$\begin{aligned} \frac{[x_D\cos(\alpha_{e_D}) - y_D\sin(\alpha_{e_D})]^2}{a_D^2} + \\ + \frac{[x_D\sin(\alpha_{e_D}) + y_D\cos(\alpha_{e_D})]^2}{b_D^2} - 1 = 0 \end{aligned} \tag{32}$$

which in polynomial form yields

$$\underline{A}_D\, x_D^2 + \underline{B}_D\, x_D\, y_D + \underline{C}_D\, y_D^2 - 1 = 0 \tag{33}$$

where

$$\underline{A}_D = \left(\frac{\cos^2(\alpha_{e_D})}{a_D^2} + \frac{\sin^2(\alpha_{e_D})}{b_D^2} \right) \tag{34}$$

$$\underline{B}_D = 2\cos(\alpha_{e_D})\sin(\alpha_{e_D}) \left(\frac{1}{a_D^2} - \frac{1}{b_D^2} \right) \tag{35}$$

$$\underline{C}_D = \left(\frac{\sin^2(\alpha_{e_D})}{a_D^2} + \frac{\cos^2(\alpha_{e_D})}{b_D^2} \right) \tag{36}$$

The equation of an ellipse might be interpreted as $y_D(x_D)$; therefore, we differentiate eq. 33 as a function of x_D to arrive at

$$\frac{\mathrm{d}y_D}{\mathrm{d}x_D} = \frac{-2\underline{A}_D x_D - \underline{B}_D y_D}{\underline{B}_D x_D + 2\underline{C}_D y_D} \, . \tag{37}$$

By setting the derivative to zero $\mathrm{d}y_{e_D}/\mathrm{d}x_{e_D} = 0$, we find the local extremum of $y_{e_D}(x_{e_D})|_{ext}$, i.e.,

$$y_D(x_D)|_{ext} = -\frac{2\underline{A}_D}{\underline{B}_D} x_D|_{ext} \tag{38}$$

for

$$x_D|_{ext} = \sqrt{-\frac{1}{\underline{A}_D - 4\underline{C}_D \frac{\underline{A}_D^2}{\underline{B}_D^2}}} \tag{39}$$

The projected radius is found from

$$r_{proj_D} = \sqrt{z_D^2 + \sin^2(\alpha_{e_D})\left(x_D^2 + y_D^2\right)} \tag{40}$$

where $\sin(\alpha_{e_D})\sqrt{x_D^2 + y_D^2}$ is the body-frame distance of the x_D-y_D plane projected onto the normal to the Sun-pointing vector $\hat{\mathbf{S}}$, i.e., the y_D-z_D plane.

Since every intersection of an ellipsoid and a plane generates an ellipse, we can conclude that the radius of the ellipsoid projected on the y-z plane is given by

$$r_{ecl} = \sqrt{(y_D(x_D)|_{ext})^2 + z_D^2} \tag{41}$$

Appendix: Grid settings used in the periodic motion search: The state space discretization used in the coarse and refined grid search studies are given in tab. C1 and tab. C2, respectively.

Table C1: Discretization of the state space in preparation for the coarse grid search

State vector element γ	γ_{min}	γ_{max}	$\Delta\gamma$
Quasi-satellite orbit around the primary - total of 20700 trajectories			
x	$-(-\mu - a_D)$	$-(1 - \mu - a_d)$	0.005
z	-0.06	0.06	0.03
$\dot{x}$	-0.05	0.05	0.025
$\dot{y} = \dot{y}(x)(1 + \delta\dot{y})$	$\delta\dot{y}_{min} = -0.1$	$\delta\dot{y}_{max} = 0.1$	$\Delta\delta\dot{y} = 0.025$
Distant orbits - total of 16335 trajectories			
x	$-(1 + \mu)$	$-(10 + \mu)$	0.075
z	-0.03	0.03	0.03
$\dot{x}$	-0.1	0.1	0.05
$\dot{y} = \dot{y}(x)(1 + \delta\dot{y})$	$\delta\dot{y}_{min} = -0.1$	$\delta\dot{y}_{max} = 0.1$	$\Delta\delta\dot{y} = 0.025$

Table C2: Discretization of the state space in preparation for the refined grid search around $[x_{ref} \;\; 0 \;\; z_{ref} \;\; \dot{x}_{ref} \;\; \dot{y}_{ref} \;\; 0]^T$

State vector element γ	γ_{min}	γ_{max}	$\Delta\gamma$
Quasi-satellite orbit around the primary			
x	$x_{ref} - 0.005$	$x_{ref} + 0.005$	0.001
z	$0.8z_{ref}$	$1.2z_{ref}$	$0.2z_{ref}$
$\dot{x}$	$\dot{x}_{ref} - 0.025$	$\dot{x}_{ref} + 0.025$	0.005
$\dot{y}$	$\dot{y}_{ref} - 0.025$	$\dot{y}_{ref} + 0.025$	0.005
Distant orbits			
x	$x_{ref} - 0.075$	$x_{ref} + 0.075$	0.015
z	$0.8z_{ref}$	$1.2z_{ref}$	$0.2z_{ref}$
$\dot{x}$	$\dot{x}_{ref} - 0.05$	$\dot{x}_{ref} + 0.05$	0.02
$\dot{y}$	$\dot{y}_{ref} - 0.025$	$\dot{y}_{ref} + 0.025$	0.005

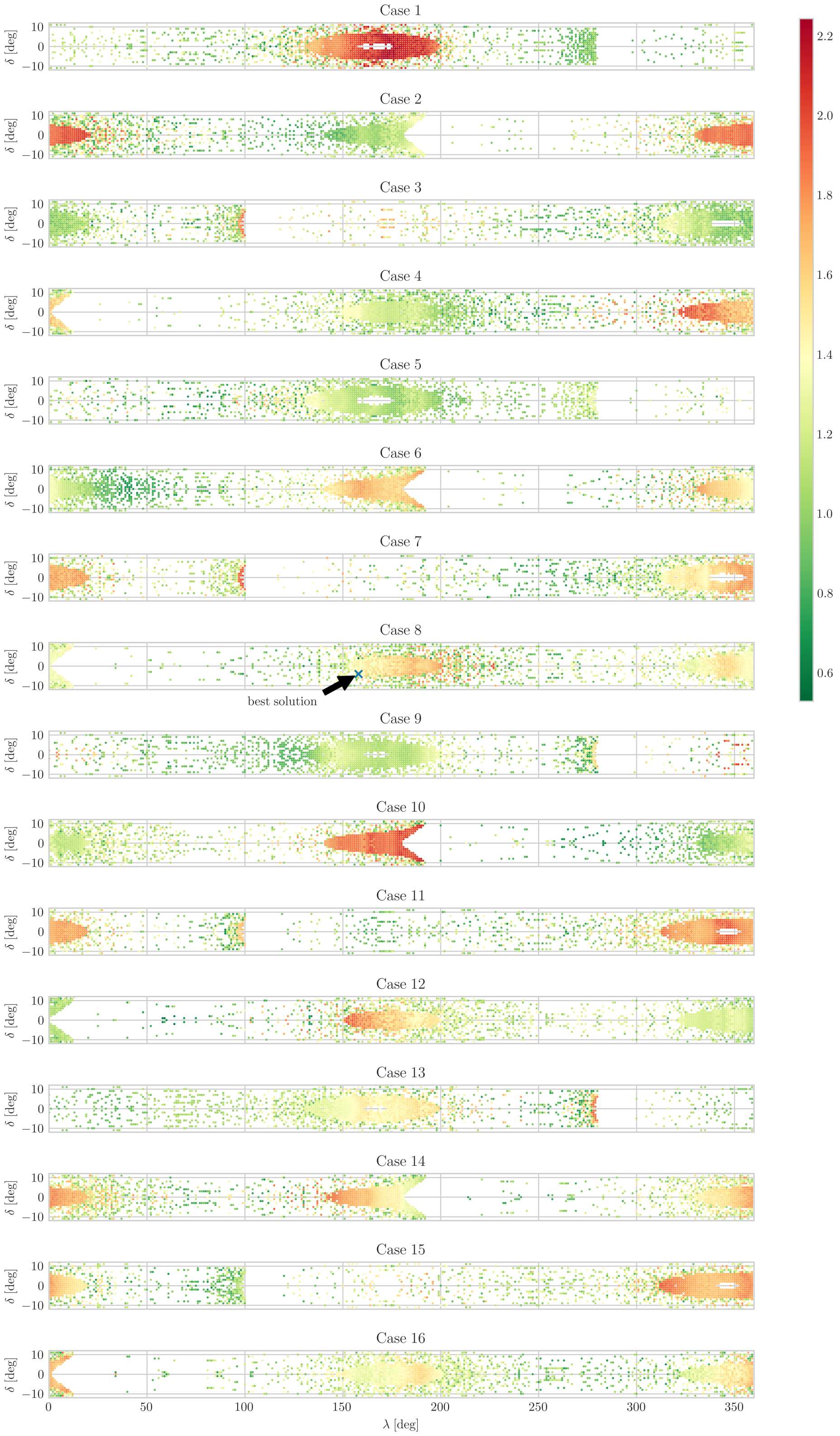

Figure 22: Distribution of capture error on the surface grid of Didymos for levitated and 'survived' particles (plotted only for the best temporary-capture candidate - DO1)

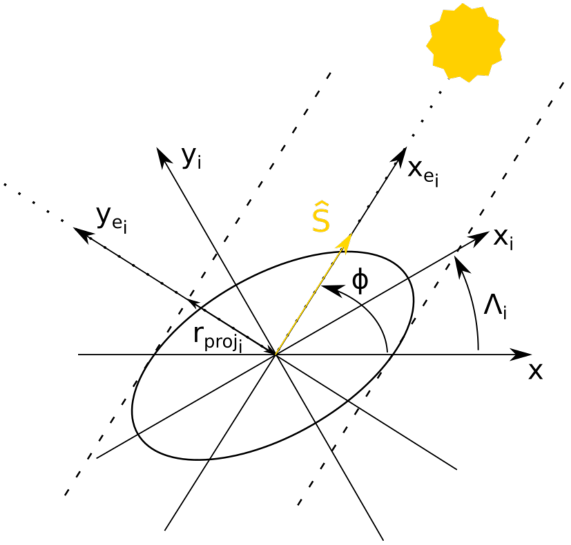

Figure 23: Quantities used in eclipse determination